REPORT DOCUMENTATION PAGE

Form Approved OMB NO. 0704-0188

1. REPORT DATE (DD-MM-YYYY)	2. REPORT TYPE	3. DATES COVERED (From - To)
22-11-2017	Final Report	1-Aug-2013 - 31-Jul-2017

4. TITLE AND SUBTITLE

Final Report: High Strain Rate Failure Modeling Incorporating Shear Banding and Fracture

5a. CONTRACT NUMBER
W911NF-13-1-0238

5b. GRANT NUMBER

5c. PROGRAM ELEMENT NUMBER
611102

6. AUTHORS

5d. PROJECT NUMBER

5e. TASK NUMBER

5f. WORK UNIT NUMBER

7. PERFORMING ORGANIZATION NAMES AND ADDRESSES

Columbia University
615 West 131st Street
Room 254, MC8725
New York, NY 10027 -7922

8. PERFORMING ORGANIZATION REPORT NUMBER

9. SPONSORING/MONITORING AGENCY NAME(S) AND ADDRESS (ES)

U.S. Army Research Office
P.O. Box 12211
Research Triangle Park, NC 27709-2211

10. SPONSOR/MONITOR'S ACRONYM(S)
ARO

11. SPONSOR/MONITOR'S REPORT NUMBER(S)
64058-EG.9

12. DISTRIBUTION AVAILIBILITY STATEMENT

Approved for public release; distribution is unlimited.

13. SUPPLEMENTARY NOTES

The views, opinions and/or findings contained in this report are those of the author(s) and should not contrued as an official Department of the Army position, policy or decision, unless so designated by other documentation.

14. ABSTRACT

15. SUBJECT TERMS

16. SECURITY CLASSIFICATION OF:			17. LIMITATION OF ABSTRACT	15. NUMBER OF PAGES	19a. NAME OF RESPONSIBLE PERSON
a. REPORT	b. ABSTRACT	c. THIS PAGE			Haim Waisman
UU	UU	UU	UU		19b. TELEPHONE NUMBER 212-851-0408

RPPR Final Report
as of 05-Dec-2017

Agency Code:

Proposal Number: 64058EG **Agreement Number: W911NF-13-1-0238**
INVESTIGATOR(S):

Name: Ph.D. Haim Waisman
Email: waisman@civil.columbia.edu
Phone Number: 21285104080000
Principal: Y

Organization: **Columbia University**
Address: 615 West 131st Street, New York, NY 100277922
Country: USA
DUNS Number: 049179401 EIN: 135598093
Report Date: 31-Oct-2017 Date Received: 22-Nov-2017
Final Report for Period Beginning 01-Aug-2013 and Ending 31-Jul-2017
Title: High Strain Rate Failure Modeling Incorporating Shear Banding and Fracture
Begin Performance Period: 01-Aug-2013 **End Performance Period:** 31-Jul-2017
Report Term: 0-Other
Submitted By: Ph.D. Haim Waisman Email: waisman@civil.columbia.edu
Phone: (212) 851-04080000
Distribution Statement: 1-Approved for public release; distribution is unlimited.

STEM Degrees: 3 **STEM Participants:** 3

Major Goals: This project aims to develop an accurate model for high strain rate failure of metals. This is accomplished through development of a new modeling framework which can capture both shear banding and fracture failure modes at the same time. Both of these modes are observed in dynamic fracture, and yet modeling of these phenomena presents numerous outstanding challenges. Among these challenges are the need to model a broad range of complex nonlinear phenomena such as multiple, possibly interacting fractures and shear bands, and at certain rates the transition from ductile to brittle failure mode. In addition, localization problems such as fracture and shear banding are challenging from a numerical perspective, requiring regularization techniques for robustness and a high resolution level to accurately reproduce the fine scale features of the solution fields. This project addresses these issues by combining a regularized shear band model with the phase field method, a framework for regularized fracture modeling. Specifically, this requires development of the combined model from thermodynamic principles, implementation of the model in a numerical code, and evaluation of the model from the perspective of experimental validation and computational efficiency.

Accomplishments: • We have proposed a novel hyperelastic formulation for shear bands at large deformations and compared it with the more common but less reliable hypoelastic formulation
• The numerical formulation of the proposed phase field - shear band model has been implemented in our FEM code and has been extended to parallel processing units
• Stability analysis of Shear bands (without cracks) has been proposed to provide more insight into the point of instability
• More efficient solvers (e.g. domain decomposition type preconditioners) for the monolithic solution of the coupled system have been proposed
• Results on one and two dimensional testing of the numerical model show improved failure modeling over a wider range of strain rates than either fracture or shear band modeling alone
• Benchmark problems (e.g. plate under high rate tension, the Kalthoff problem) have been investigated and a brittle to ductile transition was observed which is in line with theoretical and experimental observations.
• A few papers summarizing the above results and model formulation have been published and a few others are in review.
• Developed a physical stability analysis for the phase field fracture method, shearbands model and for the coupled unified shear band and fracture model.

RPPR Final Report
as of 05-Dec-2017

Training Opportunities: Two graduate students were funded by this project as listed below. Both students have graduated with a PhD degree and one student, Colin McAuliffe, continued to be supported by this project one more year as a postdoc. Furthermore, Colin McAuliffe had a successful internship with the Army Research Lab in Aberdeen Proving Ground, MD during summer of 2012.

Both students have presented their work in domestic and International conferences such as the ASCE-Engineering Mechanics Institute and US National Congress on Computational Mechanics. The two students were very successful in that their work was recognized by the community winning several awards in the field of computational mechanics. Furthermore, both students also won prestigious awards in the department for the best PhD thesis. Please see a detailed description in the Honors and Award section.

- Colin McAuliffe (former Ph.D student)
- Miguel Arriaga (former Ph.D student)

Results Dissemination: Results were disseminated through conference presentations, invited seminars and keynote lectures, posters and refereed journal publications.

Resulting Journal Publications:
- Colin McAuliffe and Haim Waisman (2015), A unified model for metal failure capturing shear banding and fracture, International Journal of Plasticity 65:131-151.
- Colin McAuliffe and Haim Waisman (2015), On the importance of nonlinear elastic effects in shear band modeling, International Journal of Plasticity 71:10-31.
- Colin McAuliffe and Haim Waisman (2016), A coupled phase field shear band model for Ductile-Brittle transition in notched plate impact, Computer Methods in Applied Mechanics and Engineering 305, 173-195, 2016.
- Miguel Arriaga and Haim Waisman (2017), Stability analysis of the phase-field method for fracture with a general degradation function and plasticity induced crack generation, Mechanics of Materials http://dx.doi.org/10.1016/j.mechmat.2017.04.003 .
- Miguel Arriaga and Haim Waisman, Combined stability analysis of phase-field dynamic fracture and shear band localization (2017), International Journal of Plasticity 96:81-119.
- Miguel Arriaga and Haim Waisman (2017), A Multidimensional stability analysis of the phase-field method for fracture with a general degradation function and energy split, Computational Mechanics, DOI 10.1007/s00466-017-1432-1.

Invited Seminars and Keynote lectures (current year):
- Seminar: Dynamic Fracture of Metals, College of Mechanics of Materials, Hohai University, Nanjing, China, July 2017.
- Keynote Lecture: Stability analysis of the Phase Field method for fracture, United States National Congress on Computational Mechanics (USNCCM14), Montreal, Canada, Jul 2017.
- Invited Lecture: A unified model for metal failure capturing shear banding and fracture, IUTAM Symposium on Integrated Computational Structure-Material Modeling of Deformation & Failure Under Extreme Conditions, Baltimore, MD, Jun 2016.
- Keynote Lecture: Stability analysis of the Phase Field method for fracture, European Congress on Computational Methods in Applied Sciences and Engineering (ECCOMAS), Crete Island, Greece, Jun 2016.
- Invited Lecture: Towards stability analysis of a unified model for metal failure capturing shear banding and fracture", IUTAM Symposium on Dynamic Instabilities in Solids, Madrid, Spain, May 2016.

Conference presentations (current year):
- An overlapping domain decomposition preconditioner for monolithic solution of shearbands, VII International Conference on Coupled problems in Science and Engineering, Rhodes Island, Greece, June 2017.
- Stability Analysis of Metals Capturing Brittle and Ductile Fracture through a Phase Field Method and Shear Band Localization, ASCE-Engineering Mechanics Institute conference, University of California San Diego, San Diego, CA, Jun 2017.
- Stability Analysis of Shear bands, ASCE-Engineering Mechanics Institute conference, Vanderbilt University, Nashville, TN, May 2016. (Presenter: Miguel Arriaga)
- Stability Analysis of Shear bands, Melosh Medal competition in Finite Element Analysis, Duke University, Durham, NC, April 2016. (Presenter: Miguel Arriaga)

RPPR Final Report
as of 05-Dec-2017

Honors and Awards: - Haim Waisman, appointed associate editor of the journal of Engineering Mechanics, January 2017.
- Haim Waisman, Associate Professor received tenure at Columbia University, April 2016.
- Miguel Arriaga, won Second Place in Computational Mechanics Poster Competition at the EMI-ASCE Engineering Mechanics Institute conference at Vanderbilt University, Nashville, TN, May 2016.
- Miguel Arriaga, Awarded the Mindlin prize for the most outstanding PhD thesis in the Civil Engineering & Engineering Mechanics department at Columbia University, May 2016.
- Miguel Arriaga, Finalist Paper in the Robert J. Melosh competition for best paper on Finite Element Methods, Duke University, NC, April 2016.
- Miguel Arriaga, won Third Place in Computational Mechanics Poster Competition at the EMI-ASCE, McMaster University, Hamilton, Ontario, Canada, August 2014.
- Colin McAuliffe, Awarded the Mindlin prize for the most outstanding PhD thesis in the Civil Engineering & Engineering Mechanics department in Columbia University, May 2014.
- Haim Waisman, Awarded the EMI Leonardo Da Vinci Award (Young Investigator), ASCE-EMI institute, August 2014.

Protocol Activity Status:

Technology Transfer: - We are currently planning to share the FEAP code with other research groups in the field. Strong collaboration has been established with a Texas A&M group (Alan Needleman and Ankit Srivastava), researchers at Sandia National Labs (Ray Tuminaro) and Los Alamos Labs (Kurt Bronkhorst).

- Once the code is validated, we also plan to share the code with interested researchers at ARL. Collaboration with ARL staff (Ryan Karkkainen and Chian Yen) has resulted in a journal publication (see below).

PARTICIPANTS:

Participant Type: PD/PI
Participant: Haim Waisman
Person Months Worked: 10.00 **Funding Support:**
Project Contribution:
International Collaboration:
International Travel:
National Academy Member: N
Other Collaborators:

Participant Type: Graduate Student (research assistant)
Participant: Miguel Arriaga
Person Months Worked: 12.00 **Funding Support:**
Project Contribution:
International Collaboration:
International Travel:
National Academy Member: N
Other Collaborators:

Participant Type: Graduate Student (research assistant)
Participant: Colin McAuliffe
Person Months Worked: 12.00 **Funding Support:**
Project Contribution:
International Collaboration:
International Travel:
National Academy Member: N
Other Collaborators:

Participant Type: Postdoctoral (scholar, fellow or other postdoctoral position)
Participant: Colin McAuliffe

RPPR Final Report
as of 05-Dec-2017

Person Months Worked: 6.00 **Funding Support:**

Project Contribution:
International Collaboration:
International Travel:
National Academy Member: N
Other Collaborators:

High Strain Rate Failure Modeling Incorporating Shear Banding and Fracture

ARO Project Final Report - Grant W911NF1310238
(Reporting Period: September 2014 - August 2017)

Haim Waisman
Civil Engineering and Engineering Mechanics
Columbia University, New York, NY 10027
waisman@civil.columbia.edu

Acknowledgement: The PI is truly thankful to the financial support of the Army Research Office under grant No. W911NF1310238, which allowed him to make contributions to high strain rate failure modeling of metals.

Contents

1 Research Objective

Understanding the failure of metals at high strain rate is of utmost importance in the design of a broad range of Army systems. Numerical methods offer the ability to analyse such complex physics and aid the design of structural systems. The objective of this research was to develop reliable finite element models for high strain rate failure modeling, simultaneously incorporating shear banding and fracture. To our knowledge, there are no such models that combine both shear bands and fracture under one unified framework, which represents a significant technical barrier to detailed failure prediction and design of material systems under high rate loading.

To this end, we have developed a computational framework that includes monolithic, mixed finite element formulation which accounts for both phenomena in a regularized continuum sense leading to mesh-insensitive results.

Shear bands are driven by shear heating caused by isochoric inelastic deformations and are regularized with thermal diffusion. Cracks propagate when the internal strain energy reaches a critical value and are regularized by using a *phase field* model, which models a crack as a diffusive entity. Both shear bands and cracks have been identified as failure modes in metals at high strain rate. We therefore contend that such a model will vastly improve quantitative failure prediction for structural components loaded at high strain rates and will support Army research with novel unified framework for shear bands and cracks.

Several Army applications in lethality and protection can be enhanced by the proposed model. Quantitative prediction of the energy absorption capability of protection systems, vehicle structures, and welded joints is extremely important for evaluation of the survivability under extreme loading conditions. Kinetic energy penetrators are another area of interest, where enhanced lethality can be achieved through quantitative prediction of self sharpening behavior. It has been observed that both fracture and shear bands are the main failure mechanisms under high rate loading. Thus, the use of numerical models which exclude either failure mechanism will tend to over estimate the energy absorption capacity. The proposed model seeks to rectify this deficiency. A particular ARL application of interest is the failure analysis of friction stir welded (FSW) aluminum joints for use in Army land vehicles. This further introduces material inhomogeneity and phase interface issues between various weld zone microstructures, all of which requires detailed dedicated analysis.

2 Introduction: Dynamic fracture and Shear Bands

2.1 Literature review

Metals and alloys subjected to dynamic loads such as impact or blast, may fail due to brittle and/or ductile fracture, shear banding, or combination of the two depending on factors such as material properties, loading rate and specimen geometry.

Fracture and shear banding are two different phenomenon in solid mechanics with distinct spatial and temporal scales. Shear bands are zones of highly localized plastic deformation, which in metals are usually observed in high strain rate loadings, while brittle/ductile cracks are material discontinuities due to cleavage and/or void coalescence.

Shear bands have also been observed in materials with non-associative flow laws like porous or

granular materials, polymers, rocks and soils [1, 2]. High strain rate loading amplifies strain rate hardening effects observed in many structural materials, which has a stabilizing effect. In contrast, thermal softening destabilizes the material as heat produced by inelastic deformation lowers the material's flow stress. The reduced flow stress then leads to more intense plastic deformation where an instability may occur. The influence of strain hardening, strain rate hardening and thermal softening produces a complex equilibrium that depends strongly on the loading rate and the material properties. Hence, thermal softening is well accepted as the main mechanism that leads to shear band formation[3–8]. However, recent studies suggest that dynamic recrystallization (DRX) may be another potential mechanism that can trigger shear band failure [9–11], but it is not considered in the current work.

While shear banding is often the main driver of failure by ductile fracture[12], it is also considered a failure mode in its own right, since the thermal softening leads to profound and rapid loss of load carrying capability [3, 13, 14].

Experimentally derived material models for these loading regimes describe plastic flow as being dependent on temperature, strain rate, and a hardening parameter [7]. While several models are available for modeling shear bands, most are similar in that increasing temperature (due to plastic work) has a softening effect which cause plastic flow to occur more readily, while increases in strain rate and the hardening parameter have a hardening effect. Following the experimental work of Marchand and Duffy [15], shear bands develop in three stages as shown in Figure 1. In Stage I, before localization, a homogeneous distribution of plastic strain is observed. Stage II begins when the thermal softening effect dominates the strain and strain rate hardening effects, resulting in strain softening, and thus mild strain localization. Stage III is marked by severe localization and rapid softening, a phenomena termed stress collapse, which indicates a sudden and large drop in the material's load bearing capability [5].

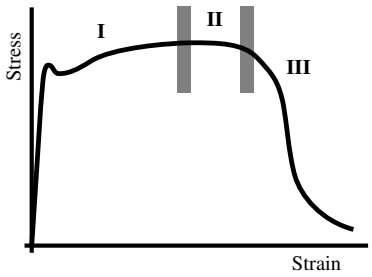

Figure 1: Stages of Shear band deformation. I-homogeneous solution, II-onset of localization, III-stress collapse.[15]

Since shear bands are typically driven by shear heating, a Taylor-Quinney(TQ) parameter is typically considered. This coefficient determines the fraction of inelastic work that is converted to heat and in most studies in the literature has been assumed to be constant with a value of 0.9. Nonetheless, recent studies indicate that the TQ coefficient is not constant and may depend on internal variables such as strain rate, plastic strain and temperature, among others. These studies assume that some portion of the plastic work goes into cold work, which is energy stored in defects within the metal's lattice [16, 17]. Following these studies we will consider in this work a generic non-constant strain-rate dependent Taylor Quinney coefficient. Note that the functional

non-linearity of the TQ coefficient is an active field of research and proper satisfactory consensus is yet to be found [16–19].

The interplay between inelastic deformation associated with shear bands and subsequent ductile fracture due to coalescence and growth of voids has been another topic of intense research. Brittle-ductile failure transition has been observed in the impact of notched plates by [20–22]. It was found that failure by shear banding occurred above a critical impact velocity, while brittle fracture resulted from lower impact velocities. While this counterintuitive phenomenon is triggered by strain rate effects, the more well known (reverse) ductile-brittle failure transition occurs due to decrease in ambient temperature[23]. Furthermore, it is interesting to note that at a transition velocity, both failure modes could be present at the same time and any reliable model should attempt to capture both modes.

Another important example is the impact and penetration of a metal plate by a projectile. In this experiment, shear bands have been identified propagating parallel to the impact direction, and cracks radiate perpendicular to the impact direction [24]. Again, both failure modes are present at the same time. These failure modes present in dynamic fracture problems involve different phenomenon with distinct spatial and temporal scales. Hence to model and characterize metals failure under dynamic loading conditions, it is thus crucial to account for all failure modes, since exclusion of any one of them neglects important underlying physics.

To this end, recent significant efforts have been made to combine the effects of plasticity and ductile fracture through the phase-field method [25, 26]. Such a model has been recently proposed by McAuliffe and Waisman [27, 28], where a unified single set of PDEs is used to capture brittle and/or ductile fracture and shear bands. In that approach, fracture is modeled with a novel phase field formulation and is coupled to the set of equations that describe shear bands [3, 13, 29–31], as illustrated schematically in Figure 2.

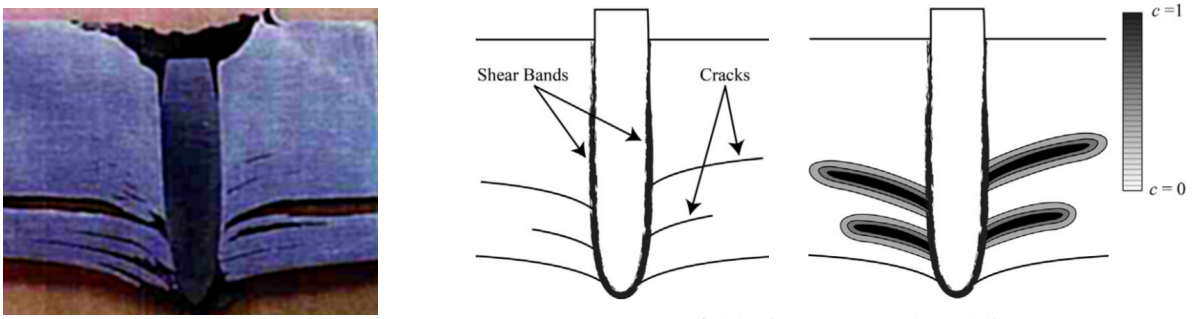

(a) Experimental Results[24] (b) Phase-field with shear band modeling[27]

Figure 2: Projectile penetrating a metal plate showing both fracture and shear localization. Figure 2a shows the experimental results of Nickodemus et al. [24] where the plate is failing due to shear deformation in the direction parallel to the penetration and cracks nucleate and propagate perpendicularly to the projectile direction. In Figure 2b, an illustration of the unified model presented in McAuliffe and Waisman [27] is depicted, where the phase field approximation to a crack is shown.

The phase-field technique is a general methodology that has been extensively used to model phase transformations in materials, particularly when dealing with problems with moving boundaries. These phases can be associated with several distinct physical phenomena, that include solidification [32–34], solid-state phase transformation [35, 36], martensitic transformation [37, 38],

dislocation dynamics [39], grain growth [40, 41], among others. In this work we use the phase-field formulation within the scope of fracture mechanics, which has been extensively studied [42–54].

As depicted in figure 3, in the phase-field formulation a crack is no longer modeled as a strong discontinuity in the domain but is instead approximated by a continuous surface density function[25, 26, 42–46, 48, 49]. The extent of the damage to the material is characterized by the phase field parameter c, which assumes the value of 1 in the fully fractured phase and 0 in the undamaged phase, and the width of the diffusive region is determined by the length scale parameter l_0 [44, 55]. This formulation has the so-called property of Γ-convergence in l_0, which means that the results will converge to standard discrete fracture mechanics results when $l_0 \to 0$[50, 56]. The value of l_0 is typically set empirically and smaller values require a larger density of elements near the crack. However, some authors have argued that l_0 should be treated instead as a material parameter and calibrated based on experimental results[57].

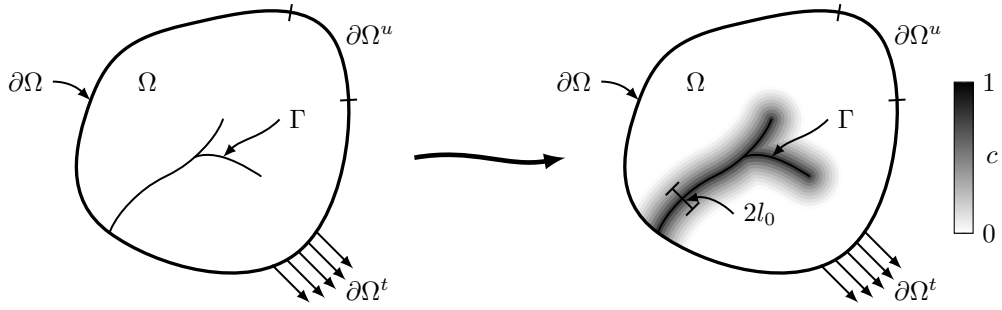

Figure 3: Schematic depiction of a solid Ω with a discontinuity Γ (crack). In the phase-field formulation the crack is simulated by the field c where a black color corresponds to a fully damaged material ($c = 1$) and a white color corresponds to a fully intact material ($c = 0$). The l_0 parameter controls the width of the process zone.

One of the most important features that control the behavior of the phase field method, is the so-called degradation function. This function is used to degrade a chosen component of the elastic strain energy (e.g. the energy associated with tension) and is typically associated with the current state of damage (i.e. the phase-field parameter).

The degradation function, denoted by $m(c)$, can be chosen arbitrarily as long as it satisfies the conditions necessary to observe Gamma convergence [56] and boundedness of the fracture force [48]. In the bulk of the work done on phase field methods, a quadratic degradation function is typically used as it is the only one for which Γ-convergence has been demonstrated [50]. However, in recent years other degradation functions have been developed [57]. For example a cubic degradation function has been suggested by Borden [58] and was shown to provide some advantages like closer resemblance to an elastic-brittle behavior as expected and obtained by traditional methods and reduction of the mild degradation that occurs away from the crack.

2.2 Modeling aspects

Given the short time scales associated with the formation of shear bands, adiabatic conditions have been commonly used in order to simplify the modeling of the problem. However, this assumption also leads to mesh-dependent results [30, 59–61]. By considering the effect of thermal diffusion,

an intrinsic length scale is introduced that functions as a localization limiter, and leads to mesh insensitive results [4, 62, 63]. Other regularization techniques reported in the literature include strain gradient theories [64–66], which have been used in the context of shear bands in [67–69] and nonlocal methods[70–72]. Mesh alignment is another form of sensitivity that can be improved using mesh-free formulations[73, 74] or Isogeometric analysis [75].

The phase-field approach results in a mathematical formulation for a diffused crack that is closely related to gradient damage mechanics [56, 76, 77], although it has been argued that this correspondence is somewhat coincidental since the approaches focus on modeling different phenomena [76, 78]. The significant difference between a phase field approach and a discrete crack approach is in the representation of a crack, continuous versus discrete, and would mostly depend on the application problem. Nonetheless, continuous representation of cracks has the advantage that it allows the functional minimization problem to be solved by numerical methods, such as the Finite Element Method, without the need for any special set of shape-functions or enrichments. Hence, complex crack patterns such as branching and coalescence can easily be captured with this approach. Even though this technique has been initially derived to tackle brittle fracture, it has also been employed to model brittle, quasi-brittle and ductile fracture combined with plasticity [27, 45, 79, 80].

In summary, two length scales are present in this model: a strong length scale l_0 dominated by fracture and a weak length scale dominated by shear bands. These length scales regularize the PDE system and have been shown to provide reliable, mesh insensitive results [81, 82].

2.3 Stability Analysis

In this work we also formulate stability conditions for a dynamic fracture and shear band localization model[27, 28]. Most of the analysis is done using the linear perturbation method but other techniques are also proposed and studied.

To motivate the stability analysis, consider that in a homogeneous problem (e.g. a bar in tension without imperfections) the phase-field formulation has two distinct behaviors. Initially, the entire problem behaves homogeneously with initiation of damage due to the driving term of the phase-field equation [83]. After a certain critical point, the system loses stability and a non-homogeneous deformation is possible, eventually leading to fracture. Hence, loss of stability provides important information and is typically associated with the onset of excessive deformation or damage and decreased reliability of the results in numerical simulations

In quasi-static simulations stability can be affected by phenomena like bifurcation due to non-associated flow law [1, 84, 85] and will limit the robustness of the numerical approach, often requiring more advanced stepping procedures (e.g. the arc-length method [86]) and regularization techniques to prevent mesh dependency in localization phenomena [4, 61, 67, 87]. In dynamic problems stability is often associated with the appearance of a non-homogeneous type of solution, for example in thermo-mechanical shearband localization [3, 88, 89].

Some examples of the importance of stability detection can be found in the work of Rabczuk et al. [90] that set strong displacement discontinuities with cohesive surfaces where local instability is detected. Song et al. [91] introduce additional tangential degrees of freedom at the discontinuity using phantom nodes. Belytschko et al. [92] inject coarse scale discontinuities based on isolating the unstable regions at the fine scale into a localization domain. Tabarraei et al. [93] use material instability based on the perturbation method to inject a phantom node discontinuity on a macro

level model based on the cohesive laws obtained from a microstructural model. Rabczuk and Samaniego [94] use instability in an adaptive mesh-free method for discontinuous modeling of shear bands. Finally, Belytschko et al. [95] set strong displacement discontinuities with a cohesive law where local instability is detected for fracture.

A popular technique for analyzing the stability of a system is the linear perturbation method which has been applied successfully to shear band problems[3, 13, 14, 63, 96–102].

We note that another popular stability approach that is widely used in the literature is based on an eigenvalue analysis of the acoustic tensor [103–106]. While the null-space criterion of the acoustic tensor has been used to study the stability of failure processes in rate independent materials, it has been suggested in the literature that this approach is not well suited for rate dependent materials (as in our case) as the equations remain elliptic [107, 108]. Therefore we choose not to pursue this route and focus on the linear perturbation method.

However, the success of the linear perturbation method comes at a significant analytical cost. New cases must undergo the laborious process of deriving a stability condition based on the governing equations and often the extension of these criteria to multi-dimensions is not trivial. Hence, in this work we also propose a method to determine the onset of shear band instability by a specially formulated local generalized eigenvalue analysis. To this end, the semi-discrete Jacobian is decomposed from its mixed finite element formulation following the derivation in [81]. Although similar techniques that compute the eigenvalues of the Jacobian matrix originated from the finite element discretization have been employed in other fields (e.g. stability of fluid dynamics [109] or thermal capillarity instability [110]), this methodology has not been employed to study local instabilities of shear bands before. It is shown that the local stability criteria based on the perturbation method mentioned above, under the same assumptions, is equivalent to the local eigenvalue analysis [88].

Like the two techniques used in this work and described above, the stability of a system is traditionally studied from the perspective of the modal spectrum of that system. The underlying reasoning is that whichever mode has the largest growth rate corresponding to an exponential growth will dominate the solution. However, for non-normal systems (i.e. systems whose eigenvectors are non-orthogonal) the short time growth-rate of a solution might not correspond to the growth rate of the most unstable mode. On the other hand, non-autonomous systems do not have a constant spectrum because of the time dependency of their operators. Since the problem being studied is neither normal nor autonomous, a generalized stability analysis is of interest [111, 112].

There are several different concepts that are important for a generalized stability analysis as shown in Farrell and Ioannou [111, 112]. The study of the growth rate of a perturbation tangent to the solution is of particular interest since it is computationally cheap and can easily be implemented on complex multiphysics systems. Additionally, an analysis based on the concept of the Rayleigh Quotient of an eigenvector is employed and is shown to also produce a good approximation of the instability point.

Albeit considerably more expensive, the local spectral analysis posses the same implementation simplicity that the instantaneous growth rate and the Rayleigh Quotient have, i.e. they only require the knowledge of the tangent stiffness matrix. However, a global modal analysis based on the eigenvalues of the full system is computationally prohibitive as the problem grows larger. This fact makes the proposed approach attractive for the study of the global instability behavior since the computational cost is of the same magnitude of the analytical instability criterion.

In the next section we summarize the research accomplishments of this project.

3 Research accomplishments

The research resulting from this project has resulted in 7 published technical paper including the following major contributions:

- A formulation that can capture fracture and shear banding in a single unified model [113]
- A novel hyperelastic formulation for shear bands at large deformations and compared it with the more common but less reliable hypoelastic formulation [114]
- Stability analysis of Shear bands, fracture and the interaction of both have been proposed to provide more insight into the point of instability [115–117]
- The unified model was discretized using finite element formulation and was implemented into a research finite element software developed in the group [28]
- A particular ARL application of interest, the failure analysis of friction stir welded (FSW) aluminum joints for use in Army land vehicles, has been studied and the findings were reported [118]
- Numerical simulations on one and two dimensional problems show improved failure modeling over a wider range of strain rates than either fracture or shear band modeling alone
- Benchmark problems (e.g. plate under high rate tension, the Kalthoff problem) have been investigated and a brittle to ductile transition was observed which is in line with theoretical and experimental observations.

Next we summarize in more details some of the research accomplishments.

3.1 A unified model for metal failure capturing shear banding and fracture

3.1.1 Summary:

In this work a thermodynamically consistent model which accounts for both shear banding and dynamic fracture and can thus capture both failure bodes at intermediate strain rates, is presented. The model consists of an elastic-viscoplastic material with strain hardening, strain rate hardening, and thermal softening. Fracture is modeled with the phase field method, for which a novel modification is presented here to account for the creation of fracture surfaces by inelastic work. Numerical examples are presented to illustrate the basic behavior of the model, and to compare it to three special cases: a damage free case, an isothermal case, and an isothermal case where the contribution of inelastic work to fracture is excluded.

3.1.2 Dynamic Fracture Governing Equations

The full set of coupled shear band and fracture PDEs that describe dynamic fracture of metals (ranging from low to high impact rates), has recently been proposed by PI-Waisman [113, 119], and is summarized under one framework, as follows:

Conservation of Momentum: $$\rho_0 \ddot{u}_i = F^{-1}_{Aj} \tau_{ij,A} \quad (1)$$

Conservation of Energy: $$\rho_0 \hat{c} \dot{T} = \kappa J F^{-1}_{Aj} F^{-1}_{Bj} T_{,AB} + \chi \bar{\sigma} g\left(\bar{\sigma}, T, \bar{\epsilon}^p\right) \quad (2)$$

Phase Field (damage) Evolution: $$c = 4 l_0^2 c_{,II} - \frac{2 l_0}{\mathcal{G}_c} \frac{\partial m}{\partial c} \left(W^+ + P^+\right) \quad (3)$$

Stress Degradation: $$\tau_{ij} = \tau^-_{ij} + m\left(c\right) \tau^+_{ij} \quad (4)$$

Flow Potential: $$\phi = \frac{\sigma_e^2}{\bar{\sigma}^2} - 1 = 0 \quad (5)$$

Inelastic Constitutive Relation: $$\dot{\bar{\epsilon}}^p = g\left(\bar{\sigma}, T, \bar{\epsilon}^p\right) \quad (6)$$

Plastic Deformation Tensor: $$\mathbf{d}^p = \left[\frac{\bar{\sigma}\dot{\bar{\epsilon}}}{\boldsymbol{\sigma} : \frac{\partial \phi}{\partial \boldsymbol{\sigma}}}\right] \frac{\partial \phi}{\partial \boldsymbol{\sigma}} = \dot{\bar{\epsilon}}^p \left[\frac{3}{2} \frac{\boldsymbol{\sigma}'}{\sigma_e}\right] \quad (7)$$

Stress Update: $$\pounds_v b^e_{il} = -2 \left(d^p_{ik} + d^t_{ik}\right) b^e_{kl} \quad (8)$$

with the appropriate boundary and initial conditions. Here the unknown fields are: u_i the displacements, $\tau_{ij} = J\sigma_{ij}$ the Kirchoff stress ($\boldsymbol{\sigma}$ is the cauchy stress and $\boldsymbol{\sigma}'$ is the deviatoric component of the cauchy stress), T the temperature, c the phase field (damage) parameter and $\dot{\bar{\epsilon}}^p$ the equivalent plastic strain. Large deformation kinematics is accounted for through the deformation gradient tensor F_{iA} and its determinant J, where the initial and current configurations are denoted by upper and lower case indices, respectively. Note that the formulation builds upon a hyperelastic formulation (as opposed to the common hypoelastic modeling approach) as presented in McAuliffe and Waisman [120] and τ_{ij} is derived from an elastic potential. Eq. (8) is an incremental kinematic update, close to the one presented by Simo and Hughes [121], where b^e_{il} is the elastic left Cauchy Green tensor, d^e_{ik}, d^p_{ik} and d^t_{ik} are the elastic, plastic and thermal rate of deformations, and $\pounds_v$ stands for a Lie derivative operator. In addition, $m(c)$ is the phase field degradation function, W^+ and P^+ are the portion of the elastic and plastic strain energies being degraded by fracture.

The particular form of $g\left(\bar{\sigma}, T, \bar{\epsilon}^p\right)$ used in the preliminary work is a thermo-visco-plastic phenomenological material model (a modified Litonski model [122]), which has the form

$$g\left(\bar{\sigma}, T, \bar{\epsilon}^p\right) = \dot{\gamma}_0 \left[\frac{\bar{\sigma}}{\sigma_0 \left(1 + \bar{\epsilon}^p/\gamma_0\right)^n \left\{1 - \delta \left[\exp\left(\frac{T - T_{ref}}{k}\right) - 1\right]\right\}}\right]^m \quad (9)$$

and describe the strong coupling between strain hardening and temperature softening. More details on quantities, material parameters and discussion on the physics (not presented here due to space limitations) can be found in [123]. Shear-banding is captured by the material model in Eq. (9) and temperature conductivity ($\kappa \neq 0$ in Eq. 2) is used to introduce a weak length scale into the system and regularize the equations. The work on shear bands regularization (without cracks), has been funded by DOE, where it was proven that thermal conductivity leads to mesh independent results, see for example [124–126]. In the current proposal, brittle and ductile fracture are captured by incorporation of the phase field method, as described in Eq. (3). In this approach, cracks are described as diffusive damage entities [127–129] (closely related to regularized gradient damage methods [130]). The complete multiphysics system accounts for plasticity, heat transfer, brittle and ductile fracture and large deformation kinematics. In this proposal our objective is to enhance

the ductile fracture component by adding a second phase field equation with a ductile length scale, which is driven by a Gurson-Tvergaard-Needleman (GTN) void growth model [131, 132].

Mixed finite element formulation has been proposed, where each equation is multiplied by a corresponding weight function and integrated over the domain. This weak form contains spatial derivatives of displacement, temperature and the phase field parameter, and therefore these three fields must be approximated by at least C^0 functions. On the other hand, spatial derivatives of the equivalent plastic strain and stresses do not appear and thus C^{-1} functions will suffice (note that a Babuska-Brezzi [133, 134] condition must be considered when developing mixed elements). The weak form is discretized in time using an implicit Newmark method where at each time step, a nonlinear problem is solved until convergence for the five fields $\mathbf{p} = [u_i \, c \, T \, \sigma_{ij} \, \dot{\bar{\epsilon}}^p]^{\mathbf{T}}$, using a monolithic Newton scheme. Such numerical approach doesn't require splitting or lagging, as opposed to most mesh sensitive explicit schemes used for these problems. Superior behaviour of the implicit scheme in terms of larger time steps, stability and accuracy has been reported in [135]. Consistent linearization of the nonlinear system leads to the following Jacobian matrix [119]:

$$\begin{bmatrix} \mathbf{M}^u_{\alpha\beta} + \mathbf{L}^u_{\alpha\beta} & \mathbf{0} & \mathbf{0} & \mathbf{K}^u_{\alpha\beta} & \mathbf{0} \\ \mathbf{W}^{cu}_{\alpha\beta} & \mathbf{M}^c_{\alpha\beta} + \mathbf{K}^c_{\alpha\beta} + \mathbf{C}^c_{\alpha\beta} & \mathbf{G}^{cT}_{\alpha\beta} & \mathbf{G}^{c\sigma}_{\alpha\beta} & \mathbf{G}^{c\bar{\gamma}^p}_{\alpha\beta} \\ \mathbf{L}^T_{\alpha\beta} & \mathbf{0} & \mathbf{M}^T_{\alpha\beta} + \mathbf{K}^T_{\alpha\beta} + \mathbf{G}^{TT}_{\alpha\beta} & \mathbf{G}^{T\sigma}_{\alpha\beta} & \mathbf{G}^{T\bar{\gamma}_p}_{\alpha\beta} \\ \mathbf{H}^\sigma_{\alpha\beta} + \mathbf{L}^\sigma_{\alpha\beta} & \mathbf{C}^{\sigma c}_{\alpha\beta} & \mathbf{G}^{\sigma T}_{\alpha\beta} & \mathbf{M}^\sigma_{\alpha\beta} + \mathbf{S}^\sigma_{\alpha\beta} + \mathbf{G}^{\sigma\sigma}_{\alpha\beta} & \mathbf{G}^{\sigma\bar{\gamma}^p}_{\alpha\beta} \\ \mathbf{0} & \mathbf{0} & \mathbf{G}^{\bar{\gamma}_p\sigma}_{\alpha\beta} & \mathbf{G}^{\bar{\gamma}_p T}_{\alpha\beta} & \mathbf{M}^{\bar{\gamma}_p}_{\alpha\beta} + \mathbf{G}^{\bar{\gamma}_p\bar{\gamma}_p}_{\alpha\beta} \end{bmatrix} \tag{10}$$

where $\mathbf{M}$ denotes mass matrices, $\mathbf{K}$ stiffness matrices arising from linear material behavior such as the Laplacian terms in the energy and phase field equations, $\mathbf{G}$ matrices arising from the derivatives of the flow law $g\left(\bar{\sigma}, T, \bar{\epsilon}^p\right)$. $\mathbf{L}$ matrices arising from nonlinear geometric behavior which arise due to the dependence of the deformation gradient, its inverse, and its determinant on the displacement, $\mathbf{C}$ arise from derivatives of the degradation function $m\left(c\right)$. $\mathbf{W}$ matrices are due to linearizing W^+ with respect to displacement. Lastly, $\mathbf{H}$ is due to linearizing the hyperelastic material law defining the stress. The structure of the Jacobian reflects the strongly coupled nature of the system of PDEs, and does not reveal any clear way to simplify or reduce the system by eliminating any of the five fields in $\mathbf{p}$. Also note that the Jacobian is not symmetric, which requires appropriate solvers.

To illustrate the potential of the proposed model we study a benchmark problem of an impact onto a notched steel plate at different velocities, also known as the Kalthoff problem [136, 137]. In these experiments, which are somewhat counterintuitive, it was observed that above a critical impact velocity, the failure is ductile, with a shear band propagating straight from the notch tip in a curved fashion. Below the critical velocity, a crack is initiated and propagates from the notch tip at about 70^{o}. Furthermore, at intermediate rates, a brittle-to-ductile failure transition is observed where both failure modes are present. These are two different failure phenomenon since shear bands are driven by shear heating caused by inelastic deformations while cracks are driven by tensile loading. We emphasize that there are currently no models that can capture both failure modes at the same time with a single model.

Preliminary results, using the dynamic fracture model proposed by the PI, are shown in Figure 5. Projectile impacts at 10, 15, 20 and 25 m/s are presented. For each impact velocity, we show the phase field parameter and the equivalent plastic strain pairs. A localized phase field value close to 1 indicate a crack (brittle fracture) while a large localization of plastic strain indicate a shear band (ductile failure). We consider a small region around the notch tip in the analysis due

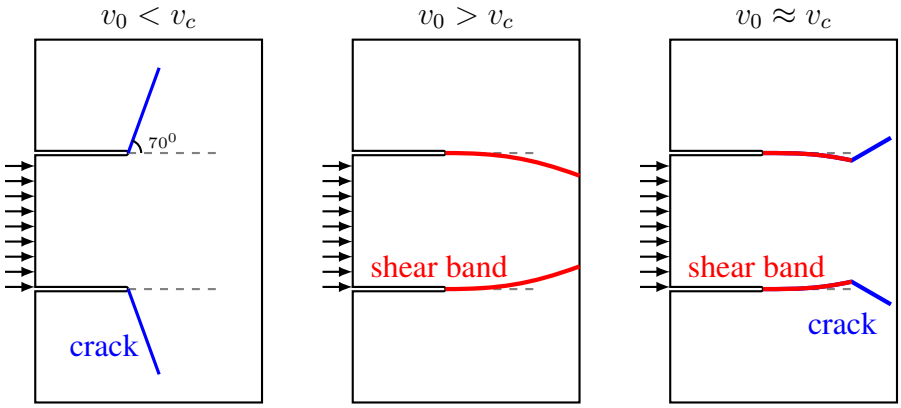

Figure 4: Impact experiments on a notched steel plate (Kalthoff problem [136, 137]). (Left) Low velocity impact leading to brittle fracture propagation from the crack tip at about 70^o. (Middle) High velocity impact with shear band forming out of the notch tip and curving inwards. (Right) Intermediate impact velocity leading to so called brittle-to-ductile failure transition with fracture initiating on top of the shearband.

to current computational limitations on the size of the problem. Nonetheless, the model is able to capture both shear bands and cracks at different strain rates. Furthermore, it is interesting to note that brittle fracture (at low impact speed) transitions to ductile fracture (at higher impact speed) with increase in strain rate. However, at this point the analysis is terminated as the nonlinear solver diverges due to severe element distortions due to the large geometric nonlinearities.

The aforementioned formulation requires a rather fine mesh in the shear band or crack path to be effective. In general, the crack and shear band paths are not known a priori, and therefore an adaptive method is needed to keep computational costs reasonable for many practical situations. For the preliminary simulations here, we fully refine the area around the notch tip, but can only capture the initiation of failure.

While initial promising results that show mesh insensitivity have been reported, validation with experiments and further discoveries are limited since more accurate micromechanics based constitutive models are needed for ductile fracture modeling. The reader may refer to [] for more details on model derivation.

3.2 Stability analysis of Shear bands and Fracture at high strain rate

In this section, we analyze the physical stability of both the fracture and the shear band failure modes and their interaction using a linear perturbation method. The analysis provides insight into the dominant failure mode and can be used as a criterion for mesh refinement.

Several numerical results with different geometries and a range of strain rate loadings demonstrate that the stability criterion predicts well the onset of failure instability in dynamic fracture applications.

For the example problems considered, if a fracture instability precedes shearbanding, a brittle-like failure mode is observed, while if a shear band instability is initiated significantly before fracture, a ductile-like failure mode is expected. In any case, fracture instability is stronger than a shear band instability and if initiated will dominate the response.

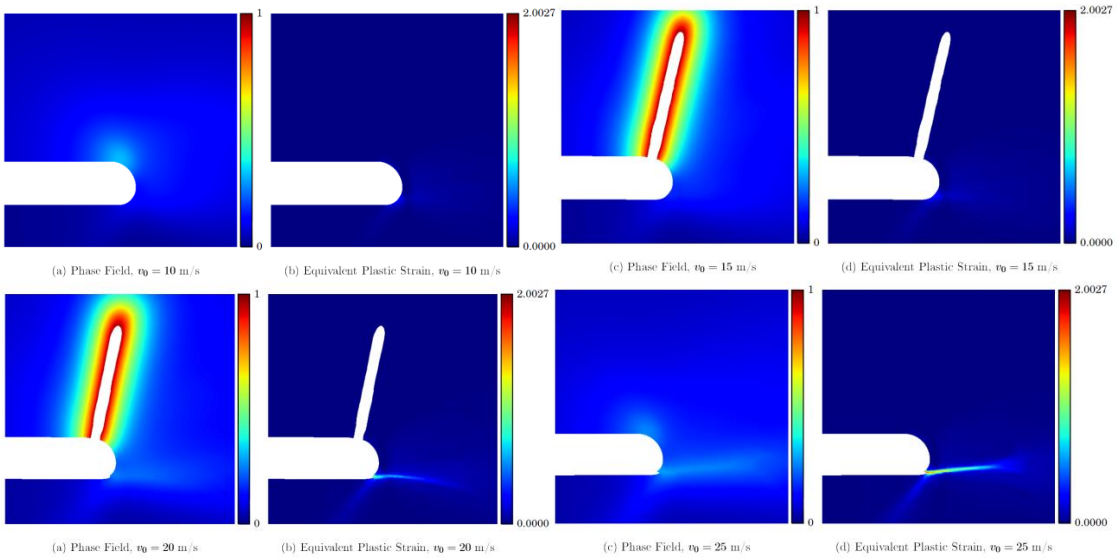

Figure 5: Numerical results of the Kalthoff experiment in Fig. 4 with projectile impacts of 10, 15, 20 and 25 m/s. For each velocity the phase field parameter and the equivalent plastic strain pairs are shown. Note how brittle fracture (at low speeds) transitions to ductile fracture (at higher speeds) with increase in strain rate.

3.2.1 Problem Statement

The dynamic fracture problem studied in this chapter consists of a thermo-mechanical system in which fracture is modeled through the phase-filed formulation, as given in equation set (1)-(8). Herein we assume a small-strain formulation for elastic-viscoplastic material models and in addition consider the 1D reduction of the model. Thus the strong-form governing equations degenerated in a 1D pure shear formulation from the multidimensional set, is as follows:

$$\text{Momentum:} \qquad \rho\ddot{u} = \tau' \tag{11}$$

$$\text{Damaged Elastic Const. Law:} \qquad \tau = G\gamma^e + [m(c) - 1]\frac{\partial W^+}{\partial \gamma^e} \tag{12}$$

$$\text{Energy balance:} \qquad \rho c_p \dot{T} = \lambda T'' + \chi\tau\dot{\gamma}^p \tag{13}$$

$$\text{Strain-Displacement:} \qquad \gamma^e = u' - \gamma^p \tag{14}$$

$$\text{Phase-Field:} \qquad \rho\theta_c\ddot{c} = G_c 2l_0 c'' - \frac{G_c}{2l_0}c - \frac{\partial m}{\partial c}(W^+ + P^+) \tag{15}$$

$$\text{Inelastic Const. Law:} \qquad \tau = P(T)Q(\gamma^p)R(\dot{\gamma}^p) \tag{16}$$

where G is the shear modulus and u' is the total strain. Note that a super-imposed dot ($\dot{x}$) corresponds to a temporal derivative and a prime (x') corresponds to a spatial derivative.

The plastic free energy that contributes to fracture, restricted to 1D, is given by

$$P^+ = \int_0^{t_0} \chi^f \tau\dot{\gamma}^p dt \tag{17}$$

Recalling the assumption of a monotonic loading and additionally assuming that all the elastic

strain is contributing to W^+, we can then specify

$$W^+ = W = \frac{1}{2}G(\gamma^e)^2 \quad \Rightarrow \quad \frac{\partial W^+}{\partial \gamma^e} = G\gamma^e \tag{18}$$

Therefore, the damaged elastic constitutive law (12) becomes

$$\tau = m(c)G\gamma^e \tag{19}$$

Additionally we neglect micro-inertia effects in the phase field equation (15), i.e. $\theta_c = 0$, and express it as

$$c = \alpha c'' - \frac{\partial m}{\partial c}\beta\left(W^+ + P^+\right) \tag{20}$$

with $\alpha = 4l_0^2$ and $\beta = \frac{2l_0}{G_c}$. The parameter α is referred to as the gradient coefficient and corresponds to the square of the characteristic length of the model. As mentioned before, $2l_0$ defines the width of the diffused crack, which means that as l_0 decreases, the value of α also decreases, making the crack narrower. The parameter β, relates the amount of energy that contributes to fracture with the critical fracture energy G_c (a material property). Therefore, the term $\beta(W^+ + P^+)$ quantifies the amount of energy with respect to G_c driving the evolution of the smeared crack and serves as the source term in the phase-field equation.

Applying the linear perturbation methodology to obtain the perturbed equations, we get

Momentum: $$\rho\delta\ddot{u} = \delta\tau' \tag{21}$$

Damaged Elastic Const. Law: $$\delta\tau = G\left(\frac{\partial m_0}{\partial c}\gamma_0^e\delta c + m_0\delta\gamma^e\right) \tag{22}$$

Energy balance: $$\rho c_p\delta\dot{T} = \lambda\delta T'' + \chi\delta\tau\dot{\gamma}_0^p + \chi\tau_0\delta\dot{\gamma}^p \tag{23}$$

Strain-Displacement: $$\delta\gamma^e = \delta u' - \delta\gamma^p \tag{24}$$

Phase-Field: $$\delta c = \alpha\delta c'' - \beta\frac{\partial^2 m_0}{\partial c^2}W_0^+(1+f_0^p)\delta c - \beta\frac{\partial m_0}{\partial c}(\delta W^+ + \delta P^+) \tag{25}$$

Inelastic Const. Law: $$\delta\tau = -P_0\delta T + Q_0\delta\gamma^p + R_0\delta\dot{\gamma}^p \tag{26}$$

where

$$f_0^p = P_0^+ \Big/ W_0^+ \tag{27}$$

$$\delta W^+ = \frac{\partial W_0^+}{\partial \gamma^e}\delta\gamma^e \tag{28}$$

$$\delta P^+ = \frac{\partial P_0^+}{\partial \gamma^p}\delta\gamma^p \tag{29}$$

and

$$P_0 = -\frac{\partial \tau}{\partial T}\bigg|_{x=x_0} \tag{30}$$

$$Q_0 = \frac{\partial \tau}{\partial \gamma^p}\bigg|_{x=x_0} \tag{31}$$

$$R_0 = \frac{\partial \tau}{\partial \dot{\gamma}^p}\bigg|_{x=x_0} \tag{32}$$

Recall that a variable with a subscript 0 corresponds to the value of that variable (or its derivatives) at the current equilibrium point which is being perturbed. For example, c_0 corresponds to the value of the phase-field c at the current equilibrium point. The spatial and time derivatives of the independent variables correspond to the multiplication of the perturbation of the independent variables by the coefficients ik and ω, respectively, i.e. $\delta x' = \mathrm{ik}\delta x$ and $\dot{\delta x} = \omega \delta x$.

Resolving all spatial and temporal differentiations through the aforementioned procedure, the independent variables can be eliminated by manipulation of (21)-(26) and the characteristic equation is obtained. Given the complexity of this result we present the characteristic equation in terms of normalized parameters, following a similar non-dimensionalization as suggested by Bai [3] for the case of adiabatic shear bands, that is

$$C_0 + C_1\tilde{\omega} + C_2\tilde{\omega}^2 + C_3\tilde{\omega}^3 + C_4\tilde{\omega}^4 = 0 \tag{33}$$

with the following expressions for the coefficients C_0, C_1, C_2, C_3 and C_4

$$\begin{aligned}
C_0 &= A_f \tilde{k}^4 \zeta \\
C_1 &= A_f \tilde{k}^2 \zeta \left(1 - B_s + A_s \tilde{k}^2\right) \\
C_2 &= C_s \left[A_f \zeta + P^g (1-\zeta)\right] + \left[A_f \zeta \left(1 + A_s\right) + 1 + P^g (1-\zeta)\right] \tilde{k}^2 \\
C_3 &= \left(1 - B_s + A_s \tilde{k}^2\right) + \left[A_f \zeta + P^g (1-\zeta)\right] \\
C_4 &= A_s
\end{aligned}$$

where

$$\tilde{\omega} = \frac{\lambda}{c_p Q_0}\omega \tag{34}$$

$$\tilde{k}^2 = \frac{\lambda^2 k^2}{\rho c_p^2 Q_0} \tag{35}$$

$$A_s = \frac{c_p R_0}{\lambda} \tag{36}$$

$$B_s = \frac{\chi \tau_0 P_0}{\rho c_p Q_0} \tag{37}$$

$$C_s = \frac{\chi \lambda P_0 \dot{\gamma}_0^p}{\rho c_p^2 Q_0} \tag{38}$$

$$\zeta = \frac{\theta - \left[\left(\frac{\partial m_0}{\partial c}\right)^2 / m_0 - \frac{(1+f^p)}{2}\frac{\partial^2 m_0}{\partial c^2}\right]\phi}{\theta + \frac{(1+f^p)}{2}\frac{\partial^2 m_0}{\partial c^2}\phi} \tag{39}$$

$$A_f = \frac{G m_0}{Q_0} = \frac{G m_0}{\frac{\partial \tau}{\partial \gamma^p}} \tag{40}$$

$$P^g = \frac{G m_0}{Q_0}\frac{\partial P_0^+}{\partial \gamma^p}\Big/\frac{\partial W_0^+}{\partial \gamma^e} \tag{41}$$

The non-dimensional regularization parameter (θ), which accounts for the effect of the perturbation length in relation with the diffused crack width (as depicted in Figure 2), is defined by

$$\theta = 1 + \alpha \mathrm{k}^2 = 1 + (2 l_0 k)^2 \tag{42}$$

and the non-dimensional source parameter (ϕ) in the phase field equation is given by

$$\phi = 2\beta W_0^+ = 2\frac{2 l_0}{G_c} W_0^+ \tag{43}$$

Note that all normalized quantities are positive with the exception of ζ.

To study the characteristic equation in (33) we employ the Routh-Hurwitz stability conditions[138, 139], which state that a fourth order polynomial will be stable, i.e. all its root are in the negative real half-plane, if the following conditions are met:

$$C_i > 0 \quad i = 0, \ldots, 4 \qquad , \qquad C_3 C_2 > C_4 C_1 \qquad \text{and} \qquad C_3 C_2 C_1 > C_4 C_1^2 + C_3^2 C_0 \tag{44}$$

Therefore, for instability to occur it is a necessary and sufficient condition that at least one of these inequalities will not be satisfied. It is important to note that once an instability condition is met, then it can be assumed that its negation is true for all subsequent analysis. Therefore, considering the limit case of $k \to 0$, there are two conditions for which the characteristic equation becomes unstable, namely

$$\zeta < 0 \quad \Rightarrow \quad \boxed{C_{PF} = \phi/\phi_c - 1 > 0} \tag{45}$$

where

$$\phi_c = \frac{1}{\frac{1}{m_0}\left(\frac{\partial m_0}{\partial c}\right)^2 - \frac{1+f_0^p}{2}\frac{\partial^2 m_0}{\partial c^2}} \tag{46}$$

and

$$\boxed{C_{SB} = 1 - B_s < 0} \tag{47}$$

where C_{PF} and C_{SB} stands for the instability criterions for fracture and shear bands, respectively.

Eigenvalue Criterion: The stability of a problem can also be analyzed from a numerical perspective by making use of the concept of Lyapunov stability where a local eigenvalue analysis of a particular partition of the element Jacobian matrix (or Tangent Stiffness Matrix) is analyzed, as presented in Arriaga et al. [88].

As Leroy and Ortiz [140] stated: "arbitrarily slow perturbations in a rate-dependent solid can only grow from quasistatic solutions." By arbitrarily slow perturbations it is understood that perturbations with small but positive growth-rate or the first eigenvalue which crosses the real half plane and becomes positive, correspond to the onset of instability.

In the current dynamic fracture model, to obtain the residual equations we first define the weak form of the governing equations by multiplying each equation in (1)-(8) by its corresponding weight function $\left[w_i^u, w_{ij}^\sigma, w^T, w^c, w^{\bar{\gamma}^p}\right]$, integrating over the problem domain and using integration by parts where necessary.

$$\mathbf{r}_u = \int_\Omega w_i^u \rho \ddot{u}_i \,\mathrm{d}\Omega + \int_\Omega w_{i,j}^u \sigma_{ij} \,\mathrm{d}\Omega - \int_\Gamma w_i^u \sigma_{ij} n_j \,\mathrm{d}\Gamma \tag{48}$$

$$\mathbf{r}_\sigma = \int_\Omega w_{ij}^\sigma \sigma_{ij} \,\mathrm{d}\Omega - \int_\Omega w_{ij}^\sigma \left[C_{ijkl}^{elas} \varepsilon_{kl}^e + [m(c) - 1] \frac{\partial W^+}{\partial \varepsilon_{ij}^e} \right] \mathrm{d}\Omega \tag{49}$$

$$\mathbf{r}_T = \int_\Omega w^T \rho c_p \dot{T} \,\mathrm{d}\Omega + \int_\Omega w_{,i}^T \lambda T_{,i} \,\mathrm{d}\Omega - \int_\Omega w^T \chi \bar{\sigma} g(T, \bar{\sigma}, \bar{\gamma}^p) \,\mathrm{d}\Omega - \int_\Gamma w^T \lambda T_{,i} n_i \,\mathrm{d}\Gamma \tag{50}$$

$$\mathbf{r}_c = \int_\Omega w^c c \,\mathrm{d}\Omega + \int_\Omega w_{,i}^c 4 l_0^2 c_{,i} \,\mathrm{d}\Omega + \int_\Omega w^c \frac{2 l_0}{G_c} \frac{\partial m}{\partial c} (W^+ + P^+) \,\mathrm{d}\Omega \tag{51}$$

$$\mathbf{r}_{\bar{\gamma}^p} = \int_\Omega w^{\bar{\gamma}^p} \dot{\bar{\gamma}}^p \,\mathrm{d}\Omega - \int_\Omega w^{\bar{\gamma}^p} g(T, \bar{\sigma}, \bar{\gamma}^p) \,\mathrm{d}\Omega \tag{52}$$

Note that the Strain-Displacement equation is not explicitly included in the weak form, but it is implicitly taken into account when computing the elastic strain in the Damaged Elastic Constitutive Law.

Accounting for the Babuska-Brezzi condition [141–143] in mixed finite element formulations, the shape functions for each field must be chosen with care. To this end, we choose C^0 piecewise linear shape functions for displacement, temperature and phase-field parameter, and C^{-1} piecewise constant functions for the stress and equivalent plastic strain.

The residual equations can be grouped into a residual vector $\mathbf{r}$ and a solution vector $\mathbf{x}$ with displacements, temperature, stress, phase-field and plastic strain as

$$\mathbf{x} = \begin{bmatrix} u_i \\ c \\ T \\ \sigma_{ij} \\ \bar{\gamma}^p \end{bmatrix} \qquad \mathbf{r} = \begin{bmatrix} \mathbf{r}_u \\ \mathbf{r}_c \\ \mathbf{r}_T \\ \mathbf{r}_\sigma \\ \mathbf{r}_{\bar{\gamma}^p} \end{bmatrix} \tag{53}$$

The coupled nonlinear problem can then be stated as

$$-\mathbf{r}(\mathbf{x}_0, \dot{\mathbf{x}}_0, \ddot{\mathbf{x}}_0) = \mathbf{M} \cdot \delta\ddot{\mathbf{x}} + \mathbf{C} \cdot \delta\dot{\mathbf{x}} + \mathbf{K} \cdot \delta\mathbf{x} \tag{54}$$

where $\mathbf{r}(\mathbf{x}, \dot{\mathbf{x}}, \ddot{\mathbf{x}})$ is the residual vector with the residual of each equation in the set of governing equations of the problem and $\mathbf{x}$ is the solution vector which contains all field variables being solved for (u_i, c, T σ_{ij}, $\bar{\gamma}^p$). $\mathbf{M}\cdot\delta\ddot{\mathbf{x}}$, $\mathbf{C}\cdot\delta\dot{\mathbf{x}}$ and $\mathbf{K}\cdot\delta\mathbf{x}$ are the obtained by computing the Gateaux differential of the residual ($\mathbf{r}$) in the $\delta\ddot{\mathbf{x}}$, $\delta\dot{\mathbf{x}}$ and $\delta\mathbf{x}$ directions as follows

$$\mathbf{M} \cdot \delta\ddot{\mathbf{x}} = \mathrm{d}_{\delta\ddot{\mathbf{x}}}\mathbf{r}(\mathbf{x}, \dot{\mathbf{x}}, \ddot{\mathbf{x}}) = \frac{\mathrm{d}}{\mathrm{d}\epsilon}\mathbf{r}(\mathbf{x}, \dot{\mathbf{x}}, \ddot{\mathbf{x}} + \epsilon\delta\ddot{\mathbf{x}})\bigg|_{\epsilon=0} \tag{55}$$

$$\mathbf{C} \cdot \delta\dot{\mathbf{x}} = \mathrm{d}_{\delta\dot{\mathbf{x}}}\mathbf{r}(\mathbf{x}, \dot{\mathbf{x}}, \ddot{\mathbf{x}}) = \frac{\mathrm{d}}{\mathrm{d}\epsilon}\mathbf{r}(\mathbf{x}, \dot{\mathbf{x}} + \epsilon\delta\dot{\mathbf{x}}, \ddot{\mathbf{x}})\bigg|_{\epsilon=0} \tag{56}$$

$$\mathbf{K} \cdot \delta\mathbf{x} = \mathrm{d}_{\delta\mathbf{x}}\mathbf{r}(\mathbf{x}, \dot{\mathbf{x}}, \ddot{\mathbf{x}}) = \frac{\mathrm{d}}{\mathrm{d}\epsilon}\mathbf{r}(\mathbf{x} + \epsilon\delta\mathbf{x}, \dot{\mathbf{x}}, \ddot{\mathbf{x}})\bigg|_{\epsilon=0} \tag{57}$$

$$\tag{58}$$

The Jacobian matrix is then constructed by approximating the rate and acceleration of the solution increment ($\delta\dot{\mathbf{x}}$ and $\delta\ddot{\mathbf{x}}$) with a Newmark-beta time-integration scheme such that (54) becomes

$$\mathbf{J} \cdot \delta\mathbf{x} = -\mathbf{r}(\mathbf{x}_0, \dot{\mathbf{x}}_0, \ddot{\mathbf{x}}_0) \tag{59}$$

where the Jacobian matrix $\mathbf{J}$ is given by

$$\mathbf{J} = \begin{bmatrix} \mathbf{M}^*_{uu} & 0 & 0 & \mathbf{K}^{\mathbf{L}}_{u\sigma} & 0 \\ \mathbf{G}_{cu} & \mathbf{K}^{\mathbf{L}}_{cc} + \mathbf{G}_{cc} & \mathbf{G}_{cT} & \mathbf{G}_{c\sigma} & \mathbf{G}_{c\bar{\gamma}^p} \\ 0 & 0 & \mathbf{C}^*_{TT} + \mathbf{K}^{\mathbf{L}}_{TT} + \mathbf{G}_{TT} & \mathbf{G}_{T\sigma} & \mathbf{G}_{T\bar{\gamma}^p} \\ \mathbf{K}^{\mathbf{L}}_{\sigma u} & \mathbf{G}_{\sigma c} & \mathbf{G}_{\sigma T} & \mathbf{K}^{\mathbf{L}}_{\sigma\sigma} & \mathbf{G}_{\sigma\bar{\gamma}^p} \\ 0 & 0 & \mathbf{G}_{\bar{\gamma}^p T} & \mathbf{G}_{\bar{\gamma}^p\sigma} & \mathbf{C}^*_{\bar{\gamma}^p\bar{\gamma}^p} + \mathbf{G}_{\bar{\gamma}^p\bar{\gamma}^p} \end{bmatrix} \tag{60}$$

with the superscript $(*)$ indicating that the matrix has been scaled by the constants that result from the time-integration scheme used. Here $\mathbf{K} = \mathbf{K}^{\mathbf{L}} + \mathbf{G}$ represents the sum of the stiffness matrices associated with linear material behavior such as elasticity and thermal diffusion ($\mathbf{K}^{\mathbf{L}}$) and the tangent stiffness matrices associated with material non-linear behavior ($\mathbf{G}$). We refer to McAuliffe and Waisman [27, 28] for additional details on this formulation.

The quasi-static finite element formulation of the system can be acquired by considering the $\mathbf{K}$ component of the Jacobain matrix, i.e. the component of the Jacobian matrix that is affecting the non-rate terms of the governing equations. Hence, the matrix $\mathbf{K}$ is given by

$$\mathbf{K} = \begin{bmatrix} 0 & 0 & 0 & \mathbf{K}^{\mathbf{L}}_{u\sigma} & 0 \\ \mathbf{G}_{cu} & \mathbf{K}^{\mathbf{L}}_{cc} + \mathbf{G}_{cc} & \mathbf{G}_{cT} & \mathbf{G}_{c\sigma} & \mathbf{G}_{c\bar{\gamma}^p} \\ 0 & 0 & \mathbf{K}^{\mathbf{L}}_{TT} + \mathbf{G}_{TT} & \mathbf{G}_{T\sigma} & \mathbf{G}_{T\bar{\gamma}^p} \\ \mathbf{K}^{\mathbf{L}}_{\sigma u} & \mathbf{G}_{\sigma c} & \mathbf{G}_{\sigma T} & \mathbf{K}^{\mathbf{L}}_{\sigma\sigma} & \mathbf{G}_{\sigma\bar{\gamma}^p} \\ 0 & 0 & \mathbf{G}_{\bar{\gamma}^p T} & \mathbf{G}_{\bar{\gamma}^p\sigma} & \mathbf{G}_{\bar{\gamma}^p\bar{\gamma}^p} \end{bmatrix} \tag{61}$$

Note that the matrix $\mathbf{K}$ is nonsymmetric and will potentially lead to complex eigenvalues.

Therefore, the stability condition based on the numerical approximation is obtained when there exists an eigenvalue of $\mathbf{K}$ with a positive real part, i.e.

$$\boxed{\text{Re}\left[\text{eig}\left(\mathbf{K}\right)\right] > 0} \tag{62}$$

The main advantage of this process is that it is straight forward to apply and will be as accurate as the FEM approximation. An implicit assumption of this method is that the values for the wave-length of the perturbation are limited to permutations of the degrees of freedom within the element discretization. In other words, the wave-lengths are locked to the element size. Nonetheless, we neglect the influence of this effect since, as mentioned earlier, the limit case is given by $k \to 0$, which corresponds to an infinitely large wave-length of the perturbation (i.e. uniform solution), which can be easily captured by the Finite Element discretization of the problem.

While this approach will be shown in the next section to agree well with both analytical criteria for shear bands and fracture, one limitation of this method is that it does not distinguish between the types of failure modes as is clearly obtained with the analytical criterion. Another drawback of the spectral method is its higher computational burden, as it requires a solution of an eigenvalue problem at each element and will slow down the analysis, which might be significant in large scale parallel computations.

3.2.2 Numerical Results

Square in tension: In this section we study the analytical criteria on a 2D formulation of an initially homogeneous system, where the effects of shear band localization and fracture are present. A homogeneous system is one where all quantities are initially constant or vary smoothly. This has the advantage that the cause for localized behavior is mostly due to the instability of the material and not due to boundary conditions or geometry.

A steel square plate is considered as shown in Figure 1 with dimension H=100μm. The plate is stretched uniaxially under a displacement control loading with v_r=0.005m/s and 5m/s, which corresponds to a nominal strain-rate of 5×10^1 s^{-1} and 5×10^4 s^{-1}.

A hyperbolic secant type imperfection is used to scale the yield stress, the hardening parameter and the critical fracture energy by a constant $\eta_{imp}(r_n)$.

The mesh consists of 50×50 quad elements, modeled by an irreducible mixed-finite element formulation with a $\overline{\text{B}}$-bar implementation to reduce shear-locking effects. As defined before, the material considered is a 4340 Steel with a Johnson-Cook constitutive law [144] with the effect of P^+ and we take into account the non-linear effects of the Taylor-Quinney coefficient as proposed by Vural et al. [19], which takes into account the influence of the isothermal conditions usually verified in quasi-static loadings.

Figure 6 shows the stress strain curve of the two different strain-rates. The stress is the average σ_{22} in the entire plate. As expected from the Johnson-Cook material law, a higher value of the strain-rate increases the yield stress of the material. Note that at this point it is not clear what type of collapse is dominating in each case.

Because a homogeneous problem is considered, the length-scales are large in comparison with the dimension of the plate being represented. This causes the stability conditions to be less localized than they would otherwise be in a problem where the length-scales are considerably smaller than the problem size. This will be seen in the Kalthoff example in the next section.

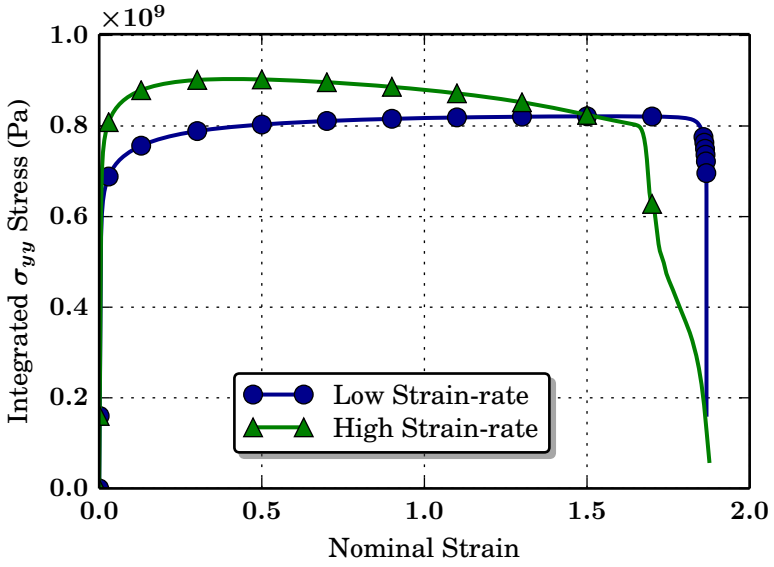

Figure 6: Stress-strain curves for both strain-rates. The low strain-rate corresponds to a value of 5×10^1 s^{-1} and the high strain-rate corresponds to a value of 5×10^1 s^{-1}.

Low Strain-rate In Figure 7 we show the stress strain curve for the low strain-rate as well as a few selected snapshot points for which a full depiction of the plate will be shown. The repeated values for the times are due to the fact that the failure process is very fast and the difference between two points in time is extremely small and approximately 0.2μs.

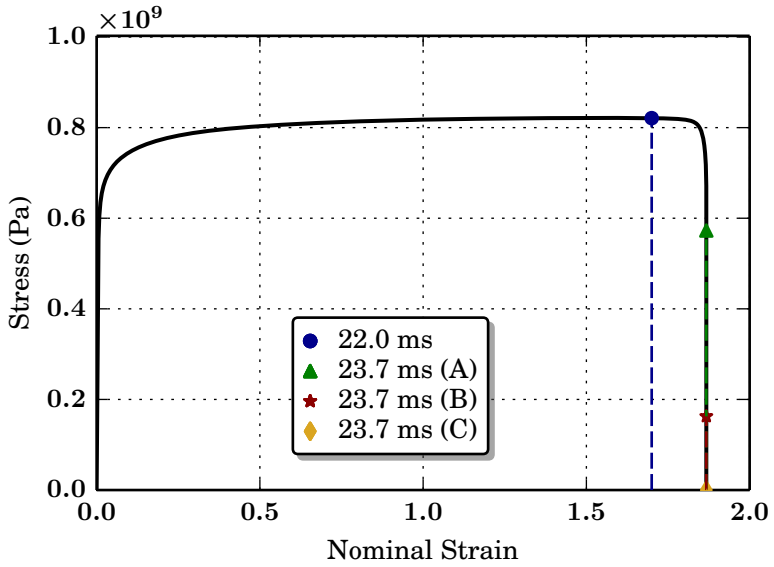

Figure 7: Stress-strain curve with the different snapshot points represented.

Figures 8-11 represent the time snapshots reporting the Phase-field parameter (c), the equiv-

alent plastic strain ($\bar{\gamma}^p$) and the instability conditions for fracture C_{PF} (Eq. 45) and shear bands C_{SB} (Eq. 47). A material region which remains stable during loading is marked by a white color while a colored region implies instability due to fracture or shear banding. Different colors show the distribution of the actual value of the instability conditions and their intensity.

The first snapshot in Figure 8 is taken near the peak stress and it can be seen that the problem only shows an instability based on a shear-band criterion. The threshold of -1 for C_{SB} delineated the region where the equivalent plastic strain is concentrating and starting to localize, although this effect is not significant as the plate has a more or less uniform distribution of the equivalent plastic strain.

The last three snapshots (Figures 9-11) show the onset of fracture, and its propagation until the complete rupture of the solid. It is interesting to note that, as the instability condition for fracture precedes and delineates the crack, the shear band instability disappears. This is a natural consequence of the unloading that occurs in the vicinity of the crack. It is also interesting to note that fracture propagates in mode I along the boundary, as would be expected at this slow strain rate.

High Strain-rate In Figure 12 we show the stress strain curve for the high strain-rate as well as a few selected snapshot points for which a full depiction of the plate will be shown.

Similarly to the previous section, Figures 13-16 represent the Phase-field (c), the equivalent plastic strain ($\bar{\gamma}^p$) and the instability conditions for fracture C_{PF} (Eq. 45) and shear bands C_{SB} (Eq. 47). For the stability conditions, a white region signifies that the material is stable while a colored region implies instability. Different colors show the distribution of the actual value of the stability conditions and their intensity.

The first snapshot in Figure 13 shows a situation that is similar to the initial snapshot of the previous section. Here, a shear band instability is visible, but unlike in the previous example, the shear band is more developed and greater inhomogeneity in the equivalent plastic strain is already visible. The threshold of -1 for C_{SB} delineates well where the localization of plastic deformation is most pronounced. Fracture is virtually non-existent with only a slight homogeneous increase in the phase field parameter and no fracture instability.

The second snapshot in Figure 14 shows a much more developed shear band. The equivalent plastic strain is localized in the 45^o direction and the C_{SB} stability condition demarcates the shear band location. A C_{PF} instability is already visible in the regions with large plastic deformation owing to the effect of P^+.

In the third snapshot represented in Figure 15, two cracks nucleate in the corners of the plate where the plastic deformation, and consequently the value of P^+, are the largest. It is interesting to note that the cracks initially propagate in mode I as can be seen in the distribution of the phase-field and in the fracture stability condition. At the same time, the shear band stability condition reverts back into a stable state near the cracks, since this region has unloaded, but the center of the plate is still uncracked and unstable from the shear band point of view.

Finally, the last snapshot is shown in Figure 16, where the crack has propagated throughout the plate causing the complete failure of the solid. The fracture stability condition recovers the full geometry of the crack and the shear band stability condition has completely subsided back into the stable regime. It is also interesting to note that fracture appears on top of the shear band and dominates the failure of the plate.

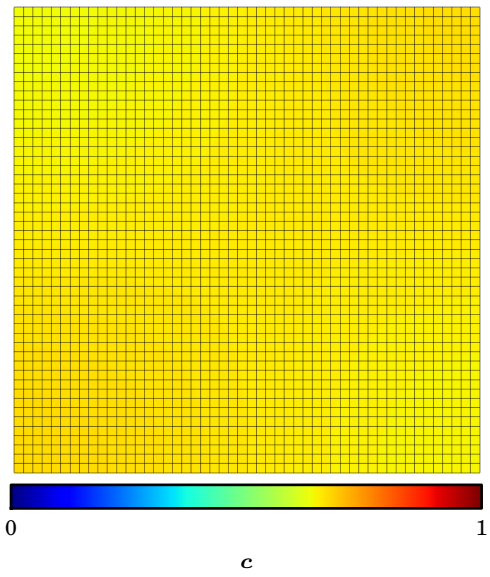

(a) Phase field parameter

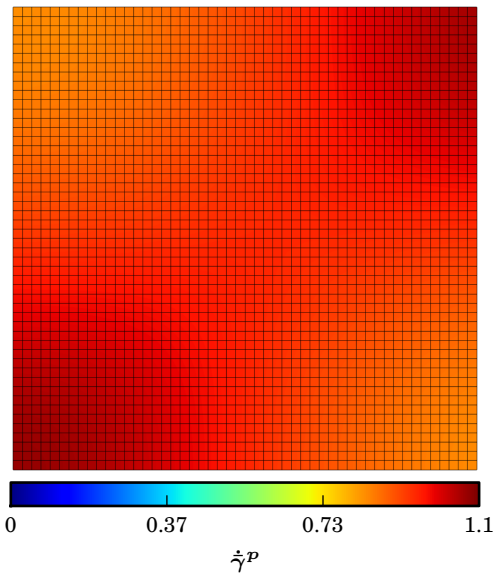

(b) Equivalent Plastic Strain

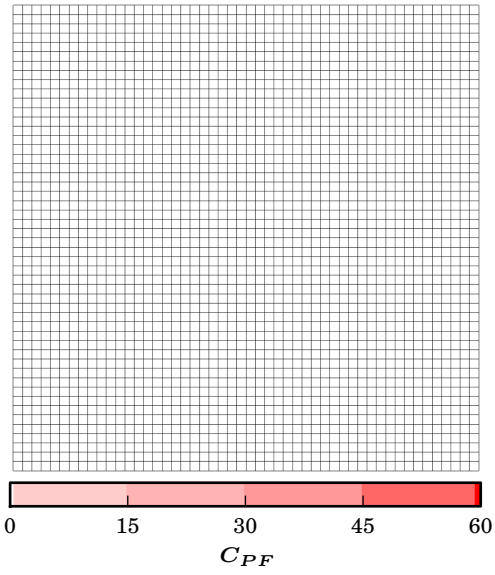

(c) Fracture instability

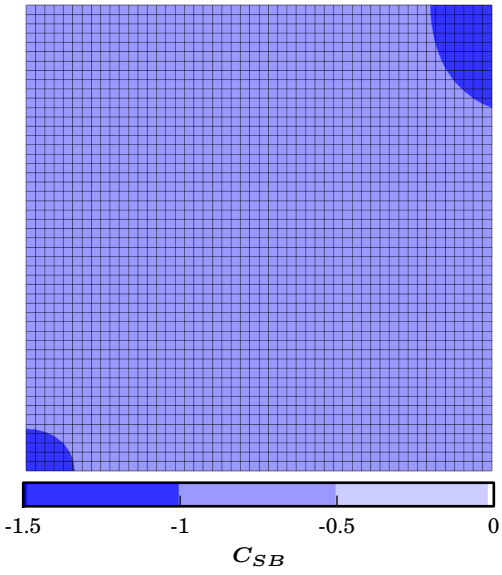

(d) Shear-band instability

Figure 8: Low Strain-rate. $t = 22.0$ms.

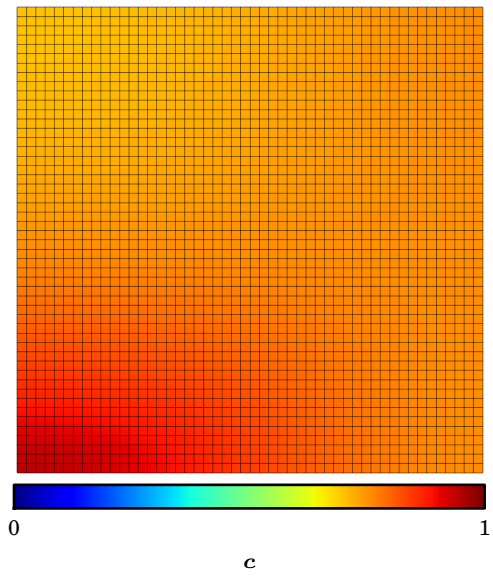

(a) Phase field parameter

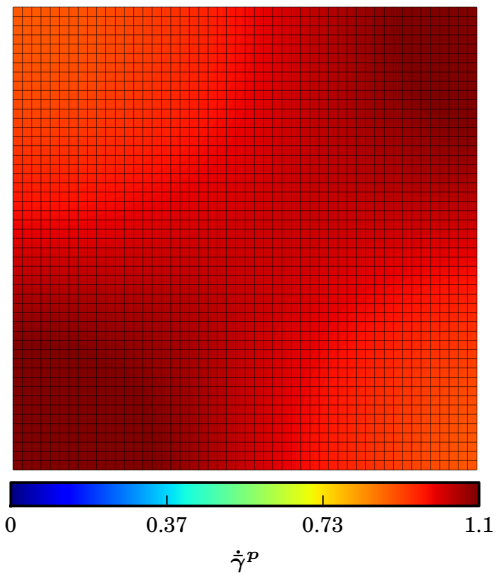

(b) Equivalent Plastic Strain

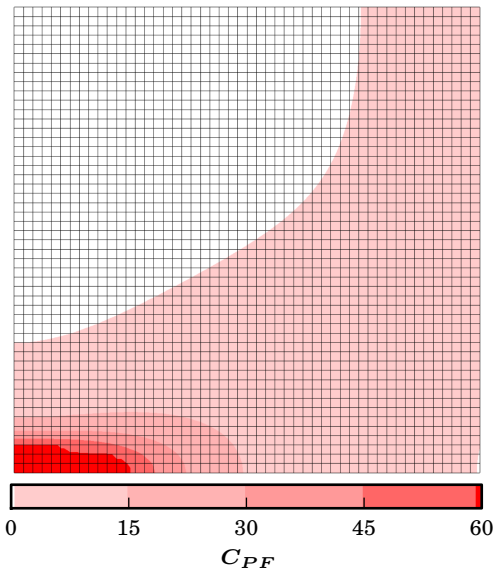

(c) Fracture instability

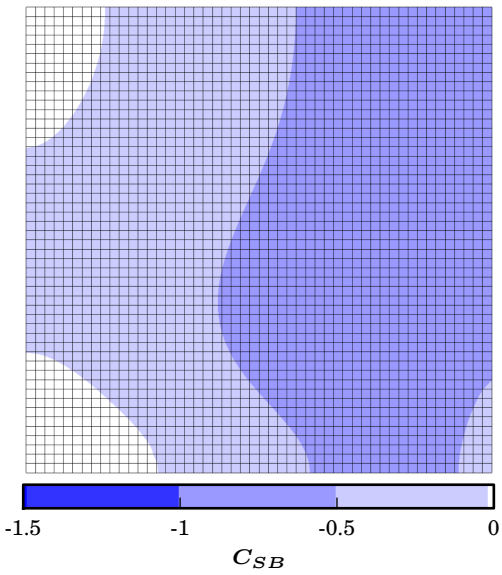

(d) Shear-band instability

Figure 9: Low Strain-rate. $t = 23.7$ms (A).

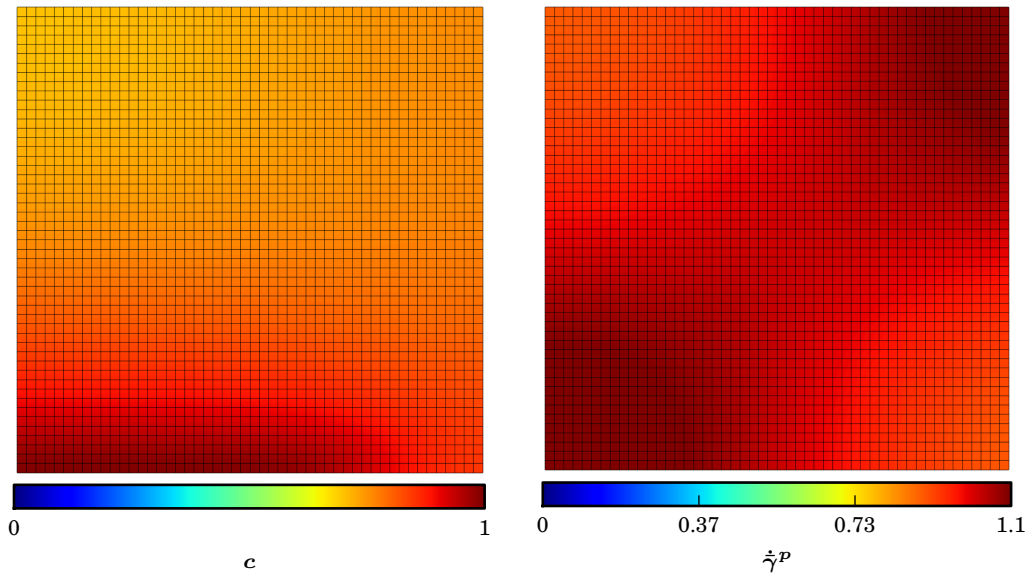

(a) Phase field parameter

(b) Equivalent Plastic Strain

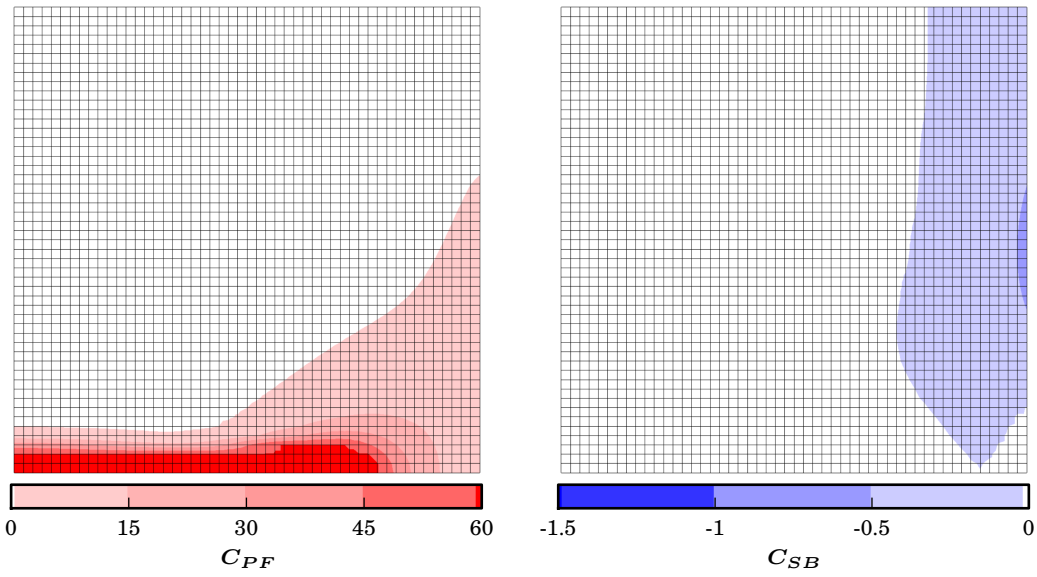

(c) Fracture instability

(d) Shear-band instability

Figure 10: Low Strain-rate. $t = 23.7$ms (B).

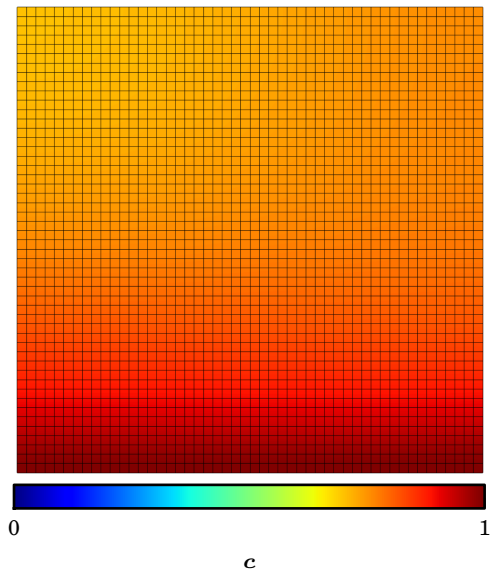

(a) Phase field parameter

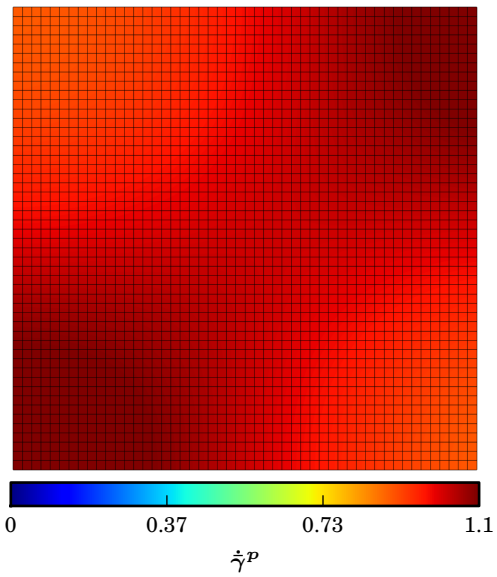

(b) Equivalent Plastic Strain

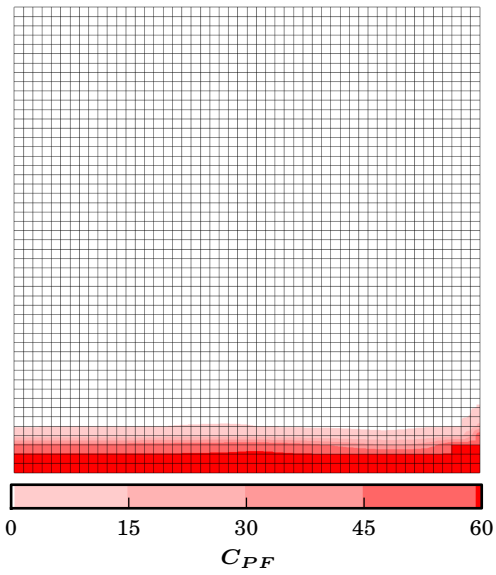

(c) Fracture instability

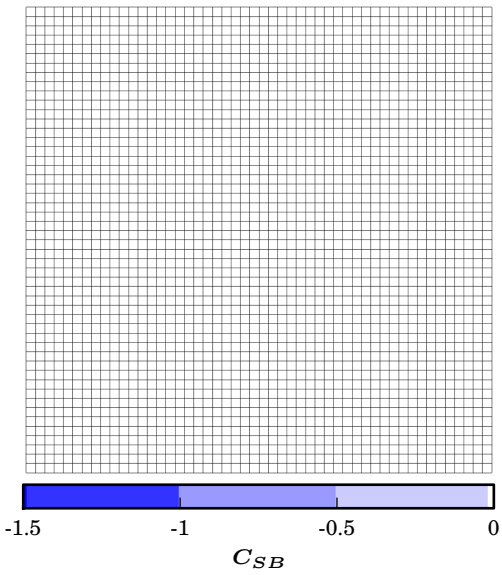

(d) Shear-band instability

Figure 11: Low Strain-rate. $t = 23.7$ms (C).

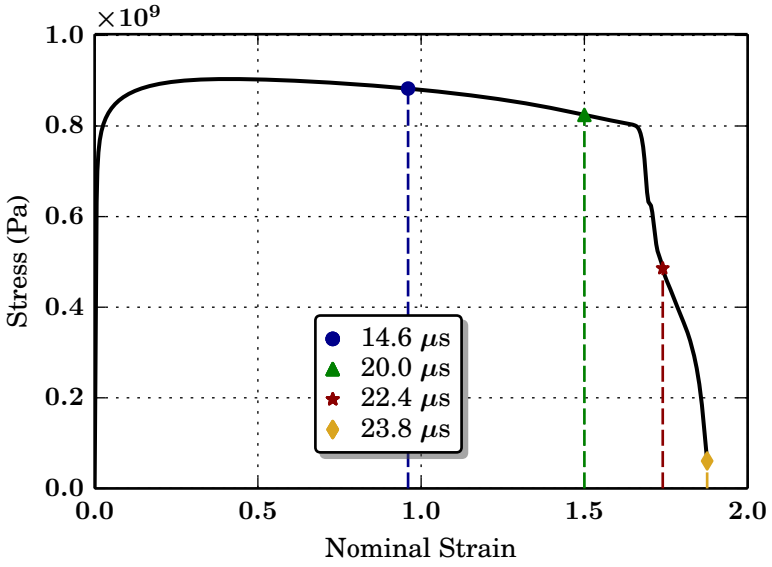

Figure 12: Stress-strain curves with different snapshots. The repeated values for the times are due to the fact that the storage of the time does not have enough precision to capture the increment between each step of 0.2μs.

Kalthoff problem In this section we study the analytical criteria on a 2D formulation of the Kalthoff problem[145] with the geometry given in Figure 17.

The material is a representative steel modeled through a combined modified version of the models of Zhou et al. [21], Areias and Belytschko [146, 147] and described in McAuliffe and Waisman [28]. The flow law is therefore given by

$$g(\bar{\sigma}, T, \bar{\gamma}^p) = \dot{\gamma}_0^p \left[\frac{\bar{\sigma}}{\sigma_0 (1 + \bar{\gamma}^p / \bar{\gamma}_0^p)^n} r(T) \right]^m \tag{63}$$

where

$$r(T) = \max \left[1 - \delta(e^{\Theta} - 1), 1 - \tanh(\delta_{ab} \Theta) \right] \tag{64}$$

with

$$\Theta = \frac{T - T_0}{k} \quad \text{and} \quad \delta_{ab} = \frac{\ln(2)}{\ln(\frac{1+\delta}{\delta})(1+\delta) - 1} \tag{65}$$

The material parameters used are given in Table 1, with a value of $G_c = 2.2E4$ kJ/m^2.

Three different velocities (v_0) are applied to the plate (15, 20 and 25 m/s) and the velocity is applied gradually over a period of 0.5μs. Henceforth these three velocities will be referred to as Low, Intermediate and High velocity, respectively.

The results are shown only in the vicinity of the notch tip, where the mesh was significantly refined. Specifically, the figures represent an area of 1×1mm^2 and the lower-left corner of the figures will be at x=50.4mm and y=112.9 mm.

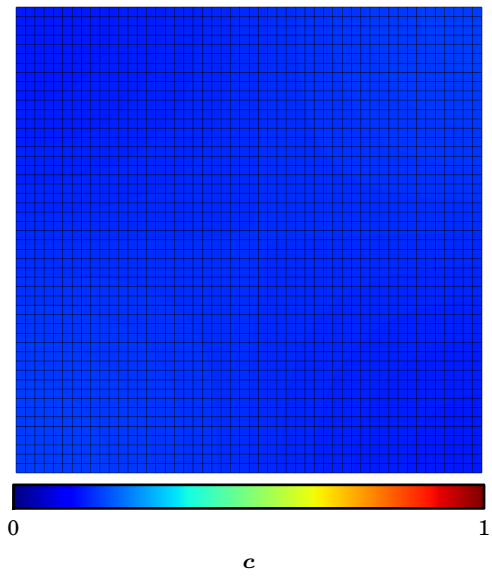

(a) Phase field parameter

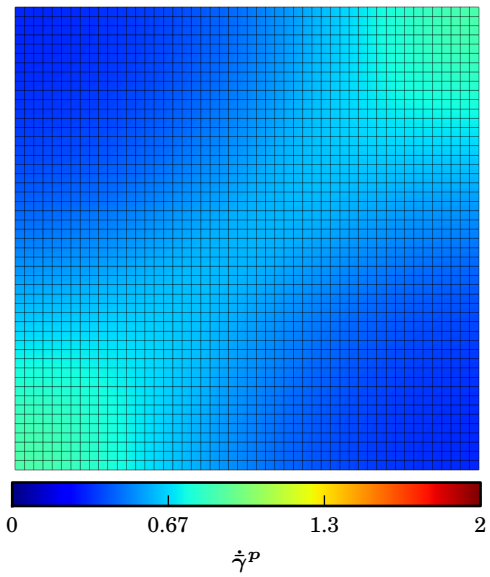

(b) Equivalent Plastic Strain

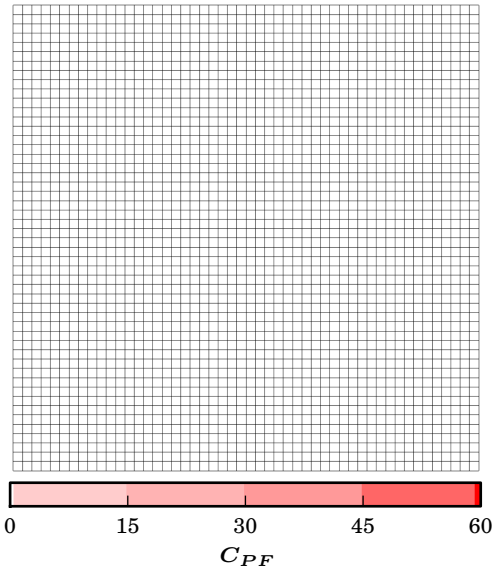

(c) Fracture instability

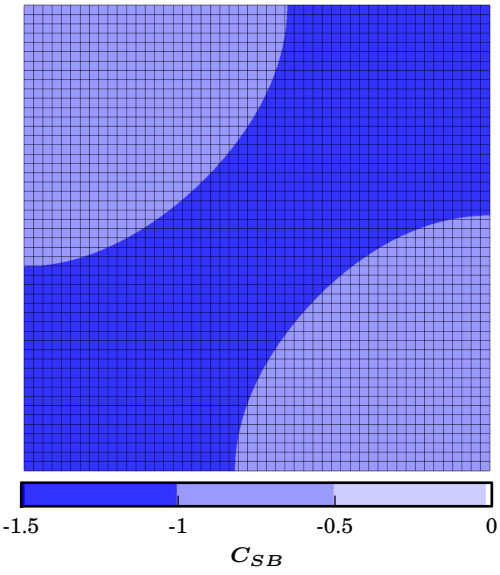

(d) Shear-band instability

Figure 13: High Strain-rate. $t = 14.6\mu$s.

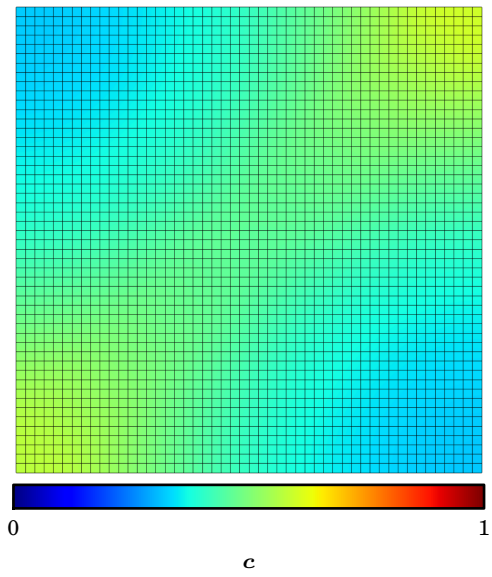

(a) Phase field parameter

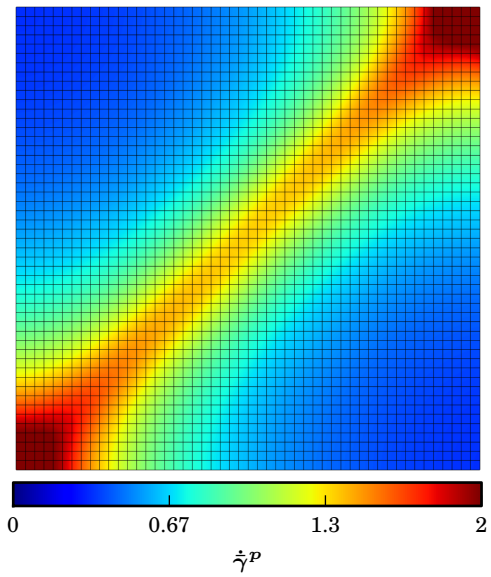

(b) Equivalent Plastic Strain

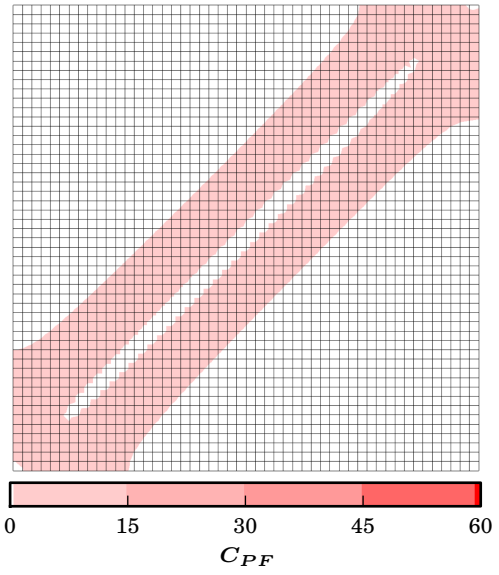

(c) Fracture instability

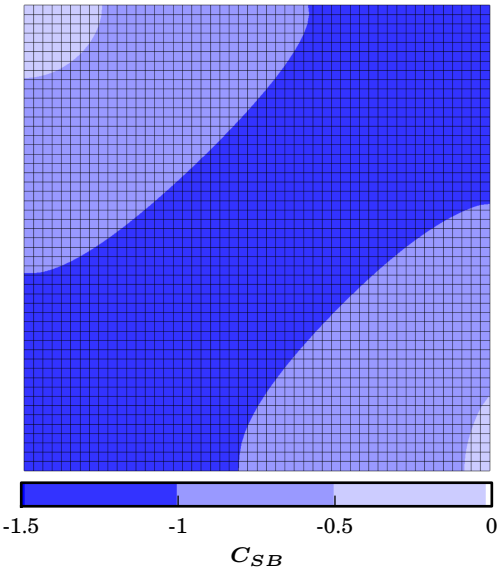

(d) Shear-band instability

Figure 14: High Strain-rate. $t = 20.0\mu$s.

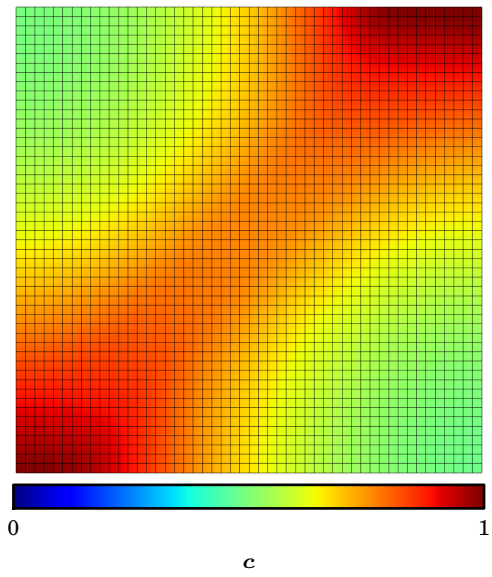

(a) Phase field parameter

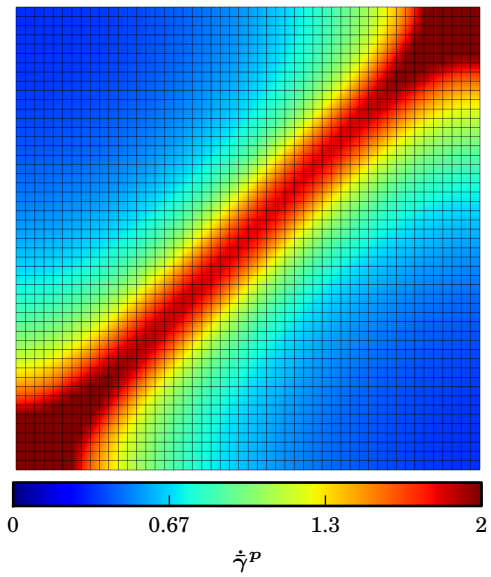

(b) Equivalent Plastic Strain

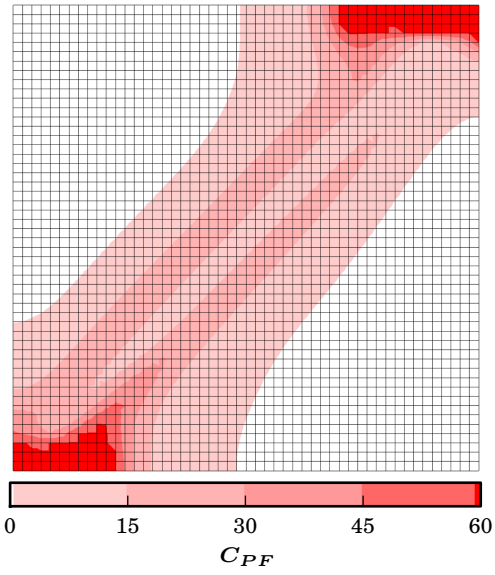

(c) Fracture instability

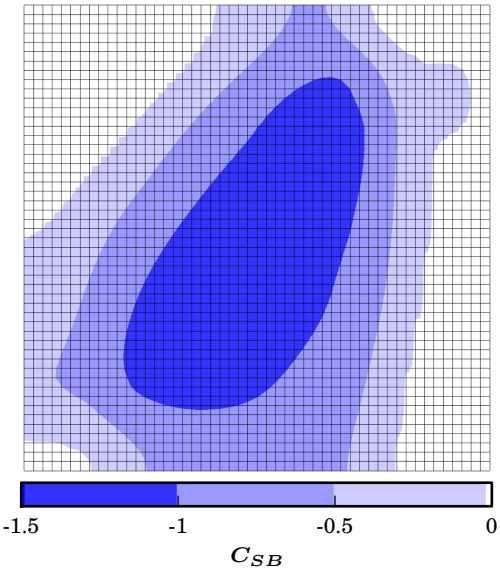

(d) Shear-band instability

Figure 15: High Strain-rate. $t = 22.4\mu$s.

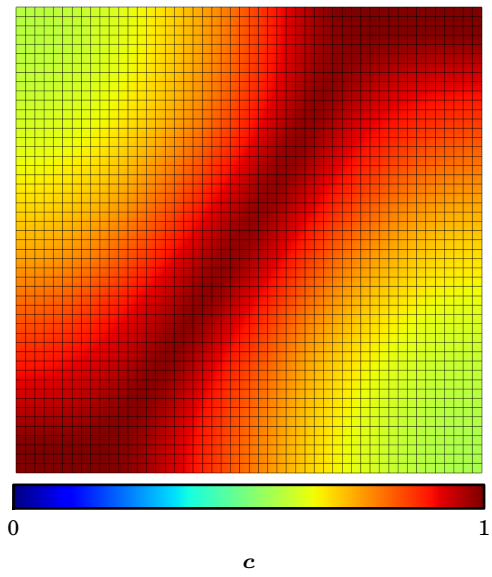

(a) Phase field parameter

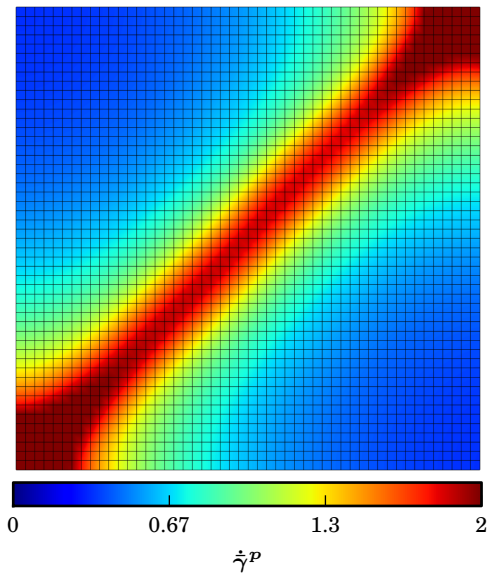

(b) Equivalent Plastic Strain

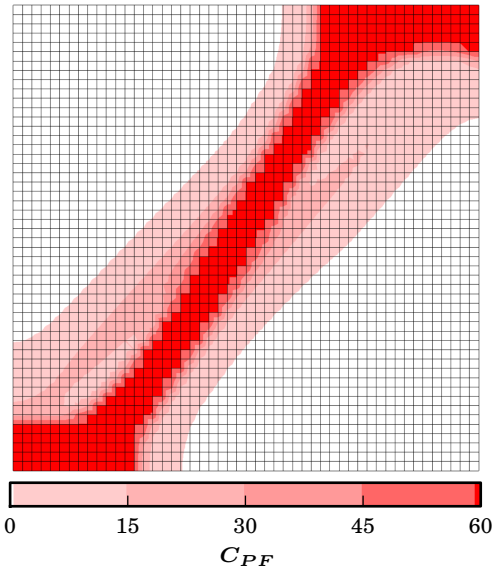

(c) Fracture instability

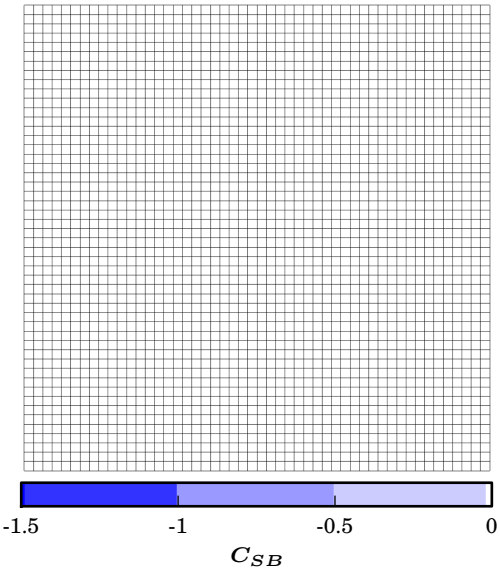

(d) Shear-band instability

Figure 16: High Strain-rate. $t = 23.8\mu$s.

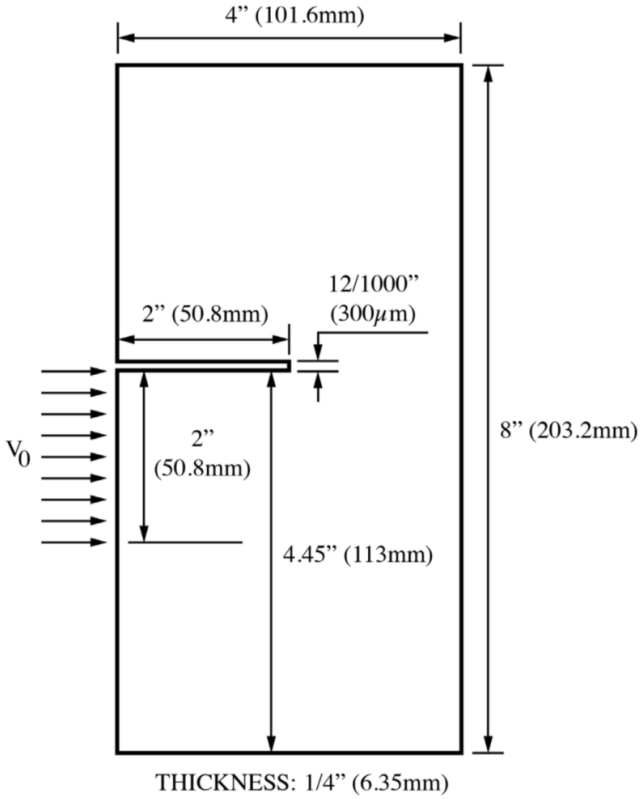

Figure 17: Full geometry of the Kalthoff Problem.

Table 1: Areias-Belytschko parameters

Property Name	Symbol	Value	Unit
Reference strain-rate	$\dot{\gamma}_0^p$	1.0	10^{-3}/s
Strain-rate hardening parameter	m	70	-
Yield stress	σ_0	2000.0	MPa
Yield strain	$\bar{\gamma}_0^p$	0.01	-
Strain hardening exponent	n	0.01	-
Reference Temperature	T_0	293	K
Thermal softening parameter	δ	0.8	-
Thermal softening parameter	k	500	K

Low Impact Velocity: Two different times are represented for this case: 27.40μs and 27.84μs. Figures 18-19 report the Phase-field parameter (c), the equivalent plastic strain ($\bar{\gamma}^p$) and the instability conditions for fracture C_{PF} (Eq. 45) and shear bands C_{SB} (Eq. 47). For the stability conditions, a white region signifies that the material is stable while a colored region implies instability. Different colors show the distribution of the actual value of the stability conditions and their intensity.

The first snapshot in Figure 18 corresponds to a point immediately before the crack starts propagating. Both the fracture instability and the shear band instability are clearly visible as both mechanisms of failure start competing. Some plastic deformation is visible in the bottom of the notch where the shear band wants to develop and the value of the phase field is clearly nucleating a crack on the upper part of the notch.

The next snapshot shown in Figure 19 illustrates an advanced stage of crack propagation . The fracture instability identifies the crack and its propagation direction and the shear band condition recovers stability due to the unloading of the crack. At this impact velocity, the contribution of thermal diffusion stabilizes the onset of the shear band and this mechanism is unable to fully develop before the crack nucleation and growth.

Intermediate Impact Velocity: Two different times are represented for this case: 25.21μs and 25.66μs. Figures 20-21 represent for this problem the same quantities as before.

The first snapshot in Figure 20 corresponds to a point immediately before the crack starts propagating. Similarly to the first snapshot in the Low impact velocity case, the fracture instability is clearly visible as well as the shear band instability. However, the shear band instability condition is now much more pronounced, with values going below the -1.5 threshold, and the shear band is clearly visible in the plot of the equivalent plastic strain. At this point the shear band localization is underway and fracture is about to initiate.

The last snapshot in Figure 21 shows an advanced stage of the propagation of the crack. The fracture instability identifies the crack and its propagation direction and the shear band condition has now significantly receded due to the unloading of the crack. The appearance of the crack has clearly halted the continuing development of the shear band as can be seen in the value of the equivalent plastic strain, which has not changed noticeably since the previous state. Nonetheless, this intermediate strain represent a case in which both fracture and shear banding processes are present at the same time.

High Impact Velocity Two different times are represented for this case: 19.66μs and 21.75μs. Figures 22-23 represent for this problem the same quantities as before.

The first snapshot in Figure 22 is taken at a moment where the development of the shear band is at a similar stage than in the first snapshot of the Intermediate velocity (Fig. 20). However, due to the higher rate of deformation, the shear band is steadily progressing and the onset of fracture instability is barely present. At this point, and unlike the previous velocity, there is not a strong indication that a crack is nucleating.

The final snapshot in Figure 23 shows an advanced stage of the propagation of the shear band. The shear band stability condition is strongly demarcating the advance of the shear band, particularly at the -1.5 threshold and the fracture stability condition is only showing mild instability. There is no apparent sign of the nucleation of a crack an the failure mechanism seems to be fully

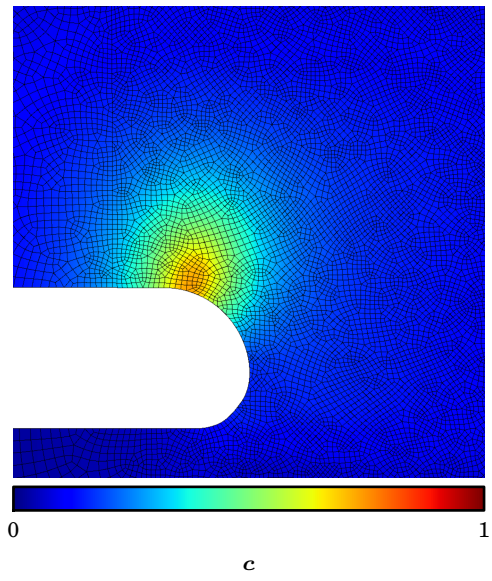

(a) Phase field parameter

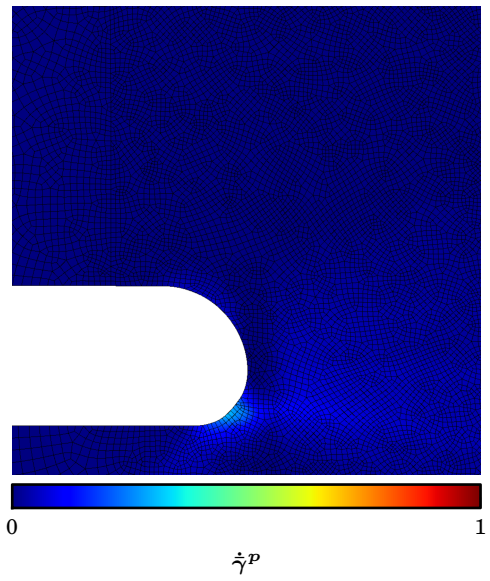

(b) Equivalent Plastic Strain

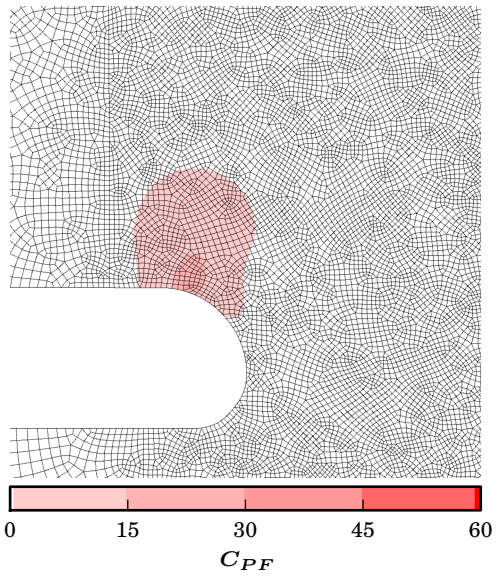

(c) Fracture instability

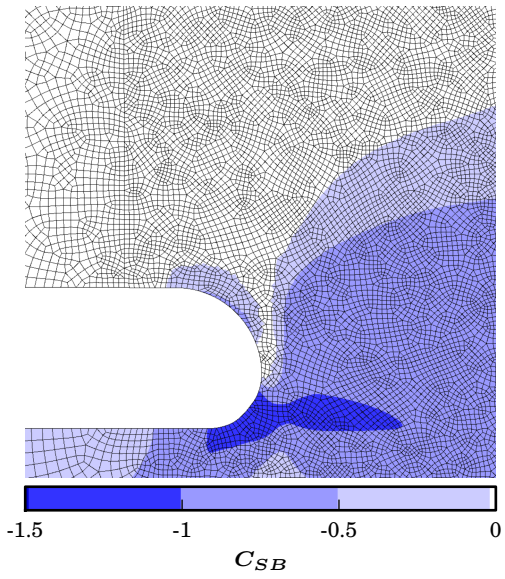

(d) Shear-band instability

Figure 18: Low Velocity. $t = 27.40\mu$s.

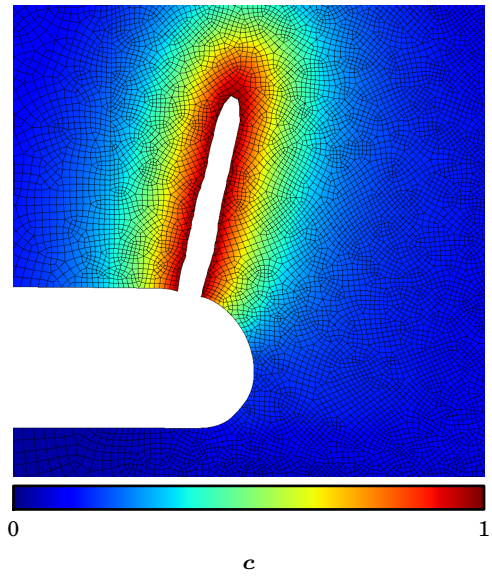

(a) Phase field parameter

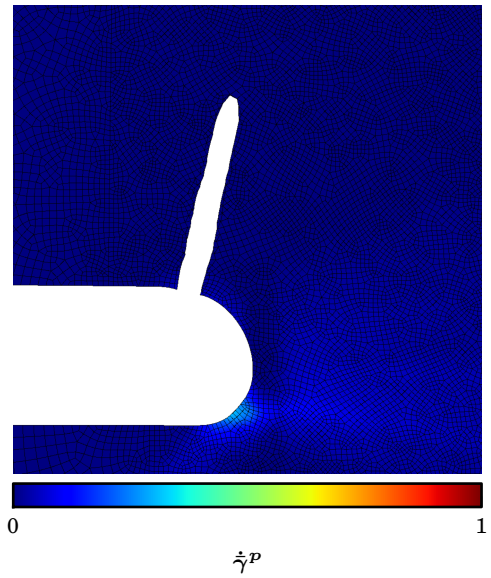

(b) Equivalent Plastic Strain

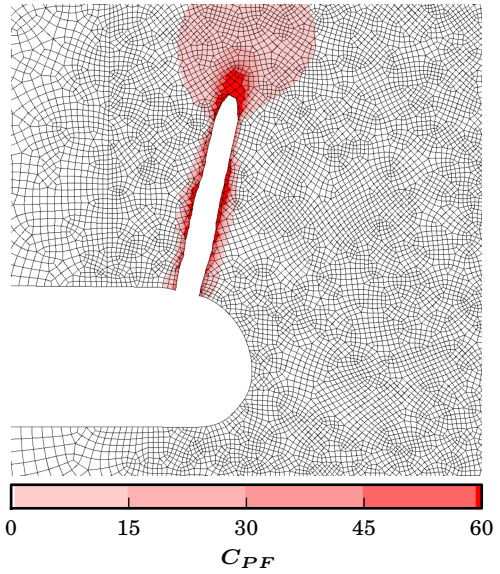

(c) Fracture instability

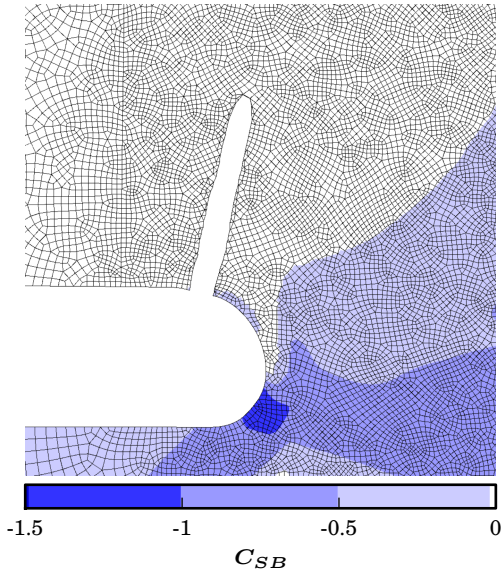

(d) Shear-band instability

Figure 19: Low Velocity. $t = 27.84\mu$s. Elements belonging to the crack (i.e. $c \geq 0.97$) were removed.

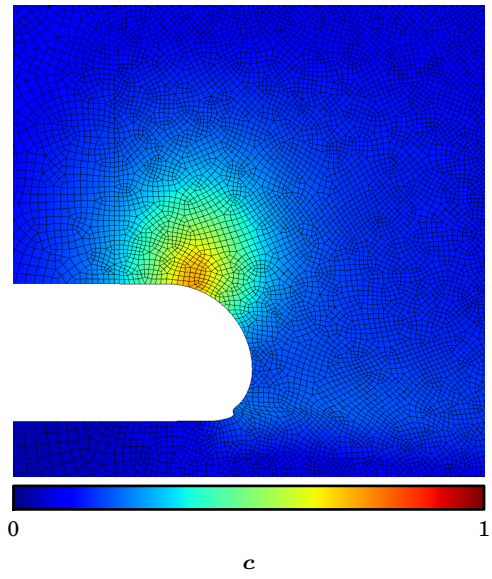

(a) Phase field parameter

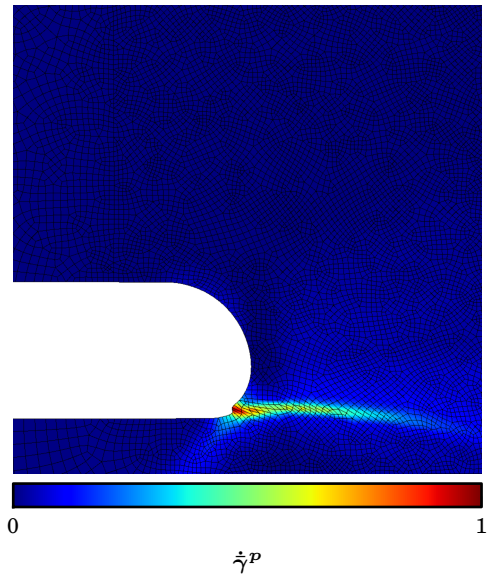

(b) Equivalent Plastic Strain

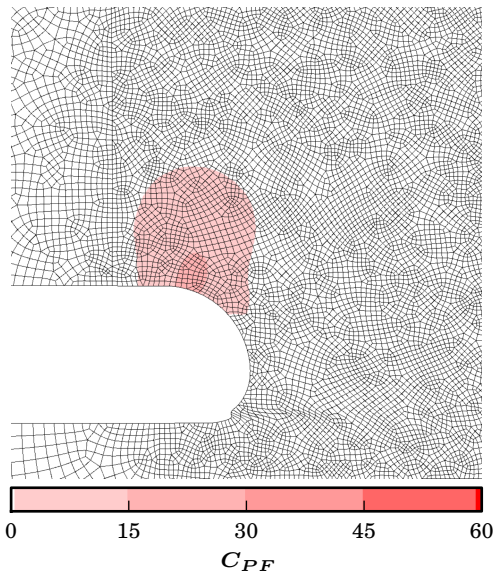

(c) Fracture instability

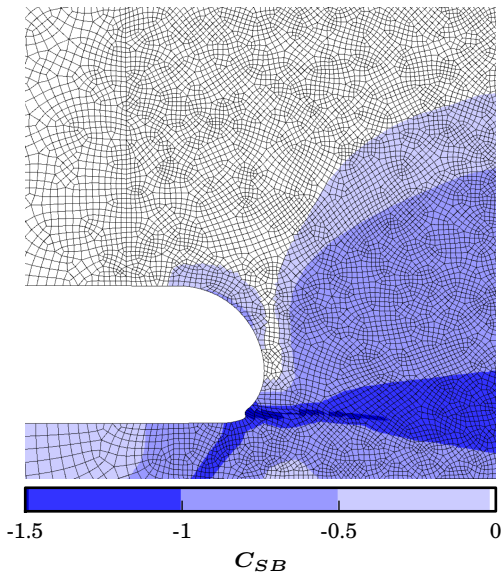

(d) Shear-band instability

Figure 20: Intermediate Velocity. $t = 25.21\mu$s. Elements belonging to the crack (i.e. $c \geq 0.97$) were removed.

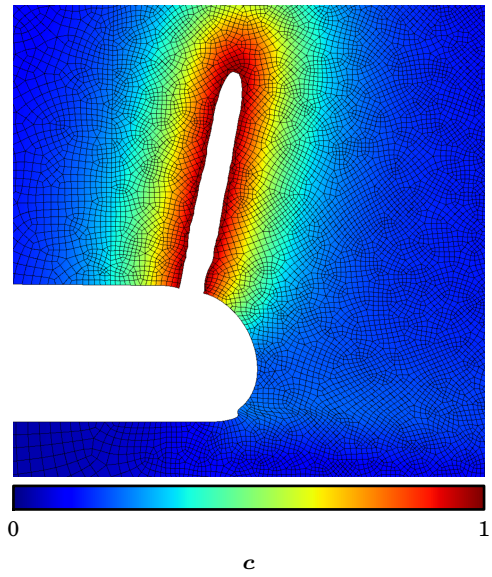

(a) Phase field parameter

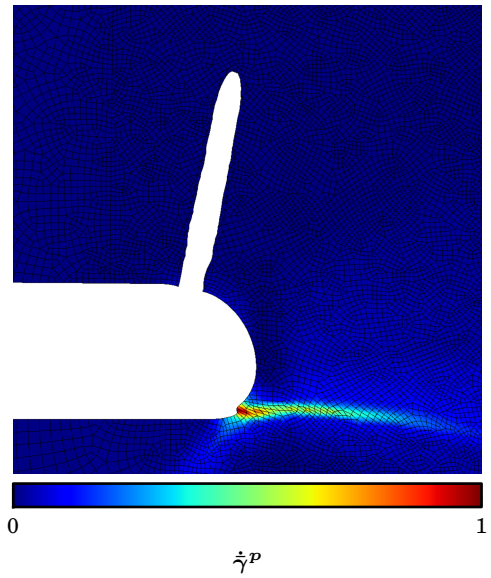

(b) Equivalent Plastic Strain

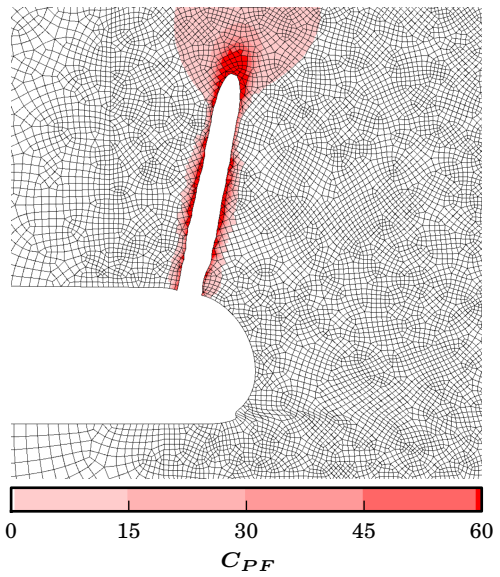

(c) Fracture instability

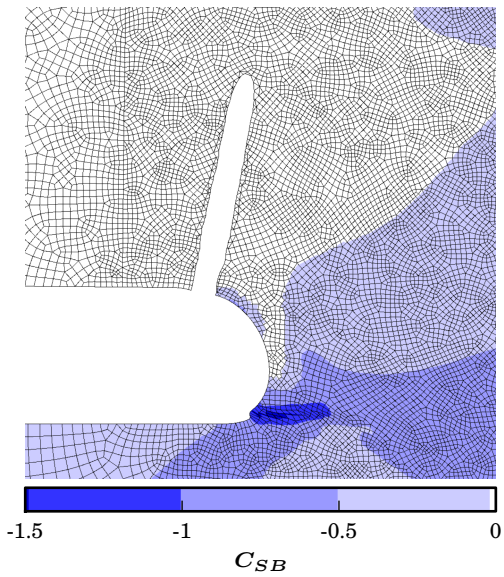

(d) Shear-band instability

Figure 21: Intermediate Velocity. $t = 25.66\mu$s. Elements belonging to the crack (i.e. $c \geq 0.97$) were removed.

dominated by shear band localization.

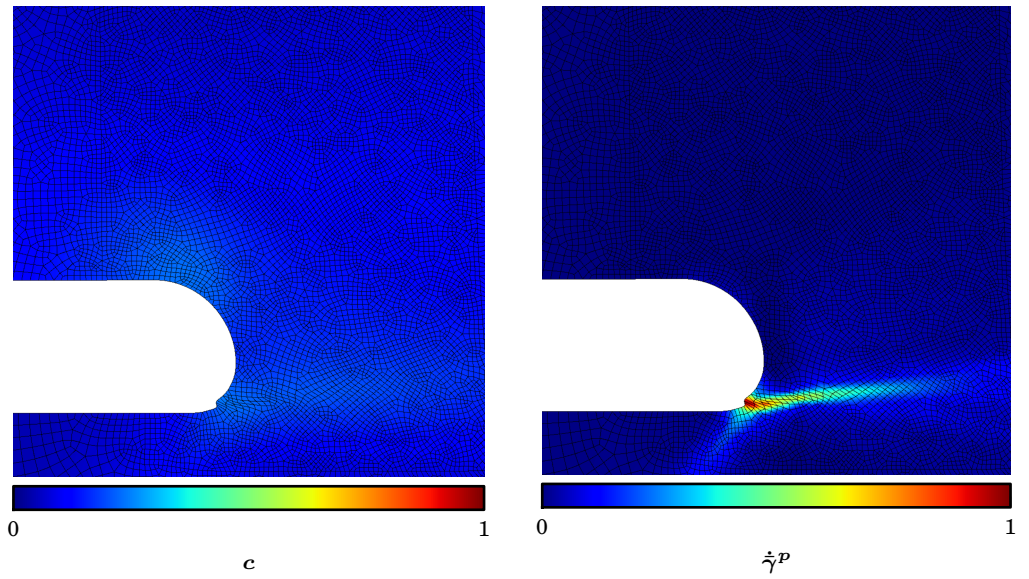

(a) Phase field parameter

(b) Equivalent Plastic Strain

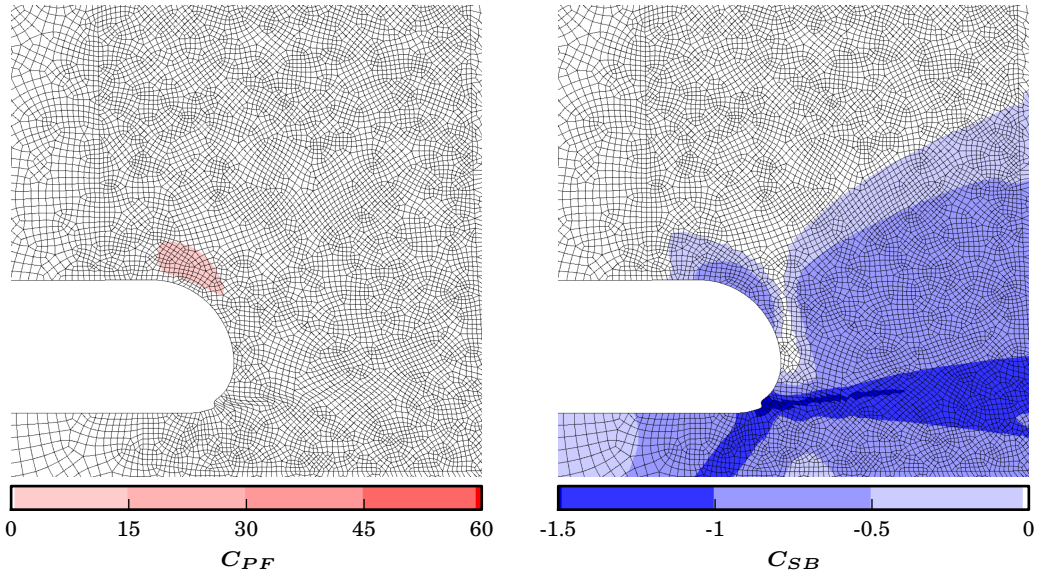

(c) Fracture instability

(d) Shear-band instability

Figure 22: High Velocity. $t = 19.66\mu$s. Elements belonging to the crack (i.e. $c \geq 0.97$) were removed.

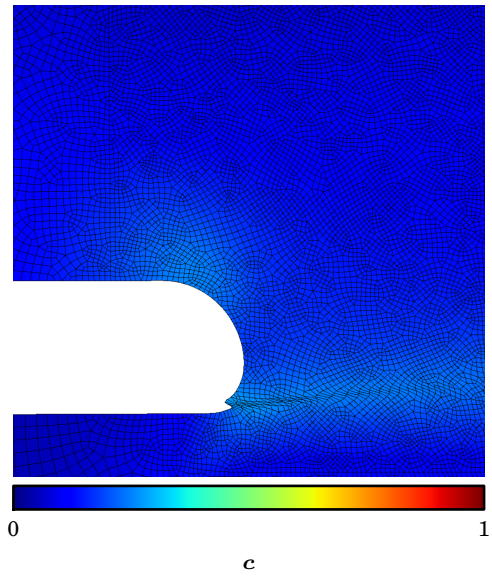

(a) Phase field parameter

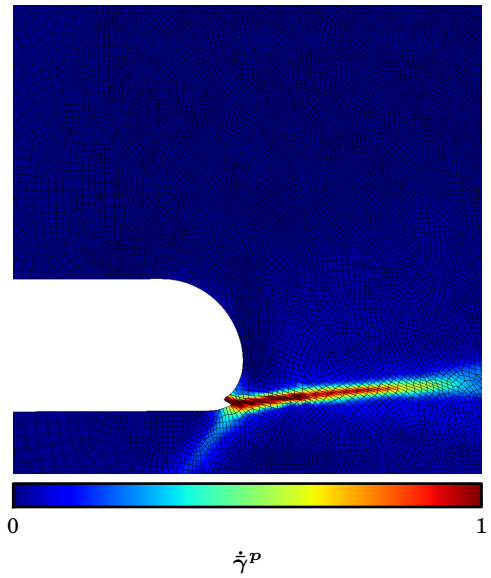

(b) Equivalent Plastic Strain

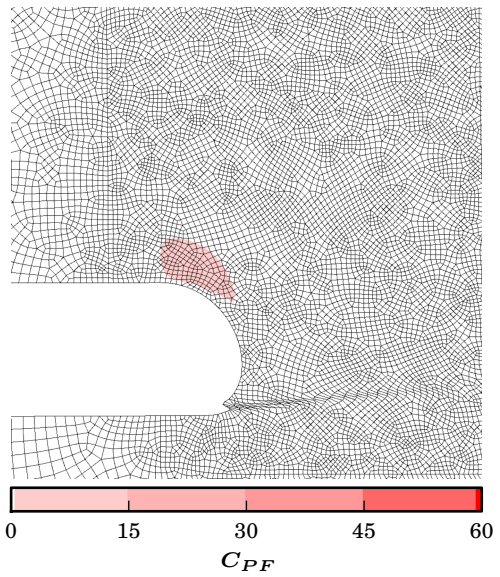

(c) Fracture instability

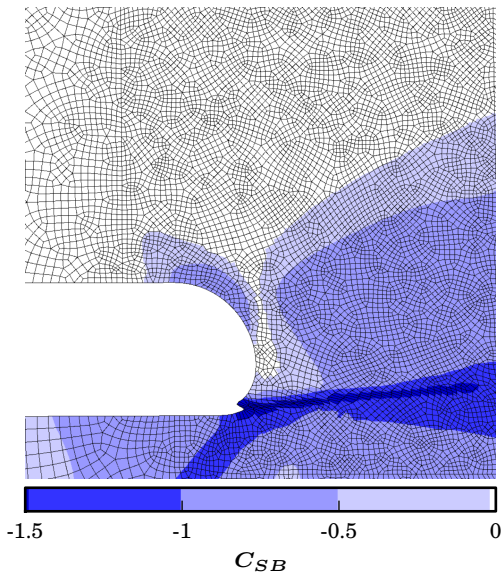

(d) Shear-band instability

Figure 23: High Velocity. $t = 21.75\mu$s. Elements belonging to the crack (i.e. $c \geq 0.97$) were removed.

3.3 Application the failure analysis of friction stir welded (FSW) aluminum joints for use in Army land vehicles

3.3.1 Summary:

Prediction of shear band formation and other strain localization processes present many computational challenges that must be overcome to enable dynamic failure prediction and material design of ductile material systems. The current work presents a finite element based computational framework accounting for this critical deformation process, as applied to a detailed investigation of friction stir welded (FSW) aluminum joints. A stir welded joint has several zones, each with distinct microstructural characteristics and material properties. For applications in Army land vehicles, which may be subject to under-body blast, an understanding of the energy absorption capability of these joints is needed. Thus material inhomogeneity, dynamic loading, and detailed understanding of small scale failure processes must all be accounted for to accurately model FSW material behavior. In this study, an implicit nonlinear consistent (INC) or monolithic solution technique is used to predict shear band formation and estimate the energy absorption and failure strain of a stir welded aluminum joint. It has been shown that failure initiating at material interface regions can be predicted, and furthermore that abrupt material property gradients predominantly contributes to FSW joint failure.

3.3.2 Friction Stir Welding (FSW)

High strength lightweight aluminum alloys offer potential advantages as replacements for traditional steels in many Army vehicles in terms of weight specific mechanical properties. Unibody chassis construction, as opposed to body on frame construction, is being pursued to lend enhanced rigidity to maintain structural integrity during potential under-body blast events. Since unibody construction requires the elimination of bolted joints, weldability of the chassis material is crucial. Alloys from the aluminum 2XXX and 5XXX series are notoriously difficult to weld with conventional techniques, but can be joined with Friction Stir Welding (FSW) [148].

FSW is a solid state joining process, which has recently been shown to be capable of producing joints in aluminum up to 76.2 mm thick [149, 150]. The FSW tool consists mainly of a shank, shoulder, and pin (shown in Figure 24), which rotate as they advance, stirring the material together. Significant inelastic deformation, heat production, and dynamic recrystallization occur during this process, which results in the formation of several zones with distinct microstructure and material properties [151–156].

Figure 25 shows a cross-section of a typical FSW joint, in this case 2139 Aluminum, which illustrates the nature of these distinct material zones. The material zone most immediately surrounding the high-torque tool pin, inserted between the welded plates, is characterized by an upper and lower weld nugget. The upper and lower weld nuggets are zones B and A respectively in Figure 25. This comes both as a direct influence of the tool pin on the material grain structure as well as the thermal properties of the material and recrystallization processes. The tool shoulder creates a great deal of friction in contact with the plate surface during the FSW process which generates an inordinate amount of heat in comparison to the bottom of the plate [157]. The difference in thermal inputs and boundary conditions thus creates a through thickness variation in recrystallization and grain growth which leads to the distinct lower and upper weld nugget, marked as

zones A and B, respectively in Fig. 25. Note, that for thin welds there is no readily discernible difference between the upper and lower nuggets, however welds of at least 2 cm thick are of the greatest interest for Army land vehicle applications. At this thickness there is a clear distinction between the upper and lower nuggets, as shown in[158, 159] Just outside of the weld nugget, zone C in Figure 25, is a third material zone which is still subject to both the mechanical and thermal influence of the FSW stirring pin. Further from the tool is a fourth material zone, too distant to be influenced by mechanical stirring, but still subject to thermal microstructural effects as heat is conducted away from the FSW joint during processing. This is known as the thermal affected zone and is marked by zone D in Figure 25. The importance of accounting for these variations must be noted, and they will play a significant role in the simulations below. Computational modeling of the FSW process, aimed at numerically predicting the FSW joint zones, have been carried out by [160–162] on joints 6.35 mm thick and by [163–165] for joint 7 millimeters thick. Additional computational studies by [166, 167] sought to determine how the FSW process parameters such as tool advancement speed affect the final weld. The studies cited above used either a Lagrangian or Arbitrary Lagrangian Eulerian (ALE) type of numerical formulation with adaptive remeshing. However, Eulerian formulations are also available [168].

In this study, we numerically model high rate loading of a small cross section of a stir welded joint. The goal is to develop a predictive capacity for energy absorption and failure of FSW joints in dynamic loading, as well as to gain an understanding of the relationship between an FSW joint microstructure and the resulting energy absorption capability and failure strain. It is found that the presence of the abruptly changing material zones leads to significantly reduced energy absorption capacity of the FSW joint in comparison to two benchmark tests with uniform material properties. The benchmarks used the material properties of the unaffected material and the lower nugget, the nominally weakest of the weld zones. This suggests that weld capacity can be improved by altering the FSW process parameters such that the final weld contains more smoothly varying zones

3.3.3 Representative Results

Cross weld tension Results of the cross weld tension simulations at two different strain rates are shown below in Figures 26-27. Figure 26 shows characteristic contour plots of equivalent plastic strain at the time of failure, and Von-Mises stress at the time of peak $\dot{\mathcal{W}}$. Contour plots are shown side by side for a uniform region of untreated aluminum followed by a plot of the simulated weld zone region in Figure 26. The shear band pattern for the UA and SW cases are clearly different, with the shear band in the SW case being contained entirely in zones 1 and 2. For the stir weld case, Yielding is first observed in the zone 2, which corresponds to the lower weld nugget. Localization is also first observed in this zone, but shear band initiation, as indicated by a precipitous drop in the local stress level during loading, originates from the upper weld nugget. This behavior is observed for both loading rates in the numerical simulation. Quasi static experiments on FSW samples reported in [158, 159] showed that the failure origin zone would be determined by which zone reaches strain hardening saturation first, which was found to be the LN. Herein we have matched these baseline quasi-static behaviors and extrapolated both to higher strain rates and a greater number of loading conditions. The dynamic case is somewhat more complicated, with rate effects and thermal softening being present. Strain hardening saturation is not an adequate indicator for failure because strain softening and localization does not necessarily imply failure, which has been noted in the experimental work of Marchand and Duffy [169], and is evident in

Figure 24: FSW tool. The tool shoulder is butted against the workpiece and the tool is rotated as it advances. This process mechanically stirs the workpiece metals together at elevated temperature, but without melting.

the numerical results presented here. The nominal strain to failure, strain energy at failure, and the zone in which failure initiates, as shown in Table 2.

Perhaps the most important feature of Figure 26 is the buildup of stresses that occur near the material zone boundary. This is essentially an interfacial stress directly due to the material inhomogeneity and property mismatch, which leads to failure of the SW joint at lower strains compared to the unaffected aluminum. This effect leads to significant differences in the overall stress strain response of the joint, which is shown in Figure 27, where the domain averaged stress σ_{22} is plotted against the nominal strain. The oscillations present in these plots are due to elastic wave reflections, which are damped quickly by plastic deformation. This illustrates that in an averaged sense, the FSW joint is marginally stronger than the lower weld nugget, but at the cost of significant ductility, failing at less than half the nominal strain of the untreated aluminum. The loss of mechanical capacity of the weld can clearly be seen in comparing the FSW weld performance (SW) to that of unwelded aluminum (UA) in Figure 28. The FSW joint fails at approximately 5 times lower mechanical energy for the strain rate of 1E3 s^{-1} and 3 times lower for the rate of 1E4 s^{-1}, due both to softening (and lower initial rate of strain energy) and a lower strain capacity before failure initiation see Table 2. Though thermo-mechanical property degradation due to FSW processing clearly weaken the FSW joint strength, it is readily apparent that inhomogeneity of the joint and interfacial stress risers are the key drivers for loss of mechanical capacity. This is evidenced by the fact that if the entire region were comprised of the nominally weakest material of the lower weld nugget, this would still outperform the actual FSW. This comparison is clearly seen in Figure 28, in which the rate of strain energy is comparable, yet the duration of significant energy absorption prior to failure is much larger for monolithic LN material as compared to the actual FSW joint. The reduction in energy absorption at the strain rate of 1E3 s^{-1} is greater than

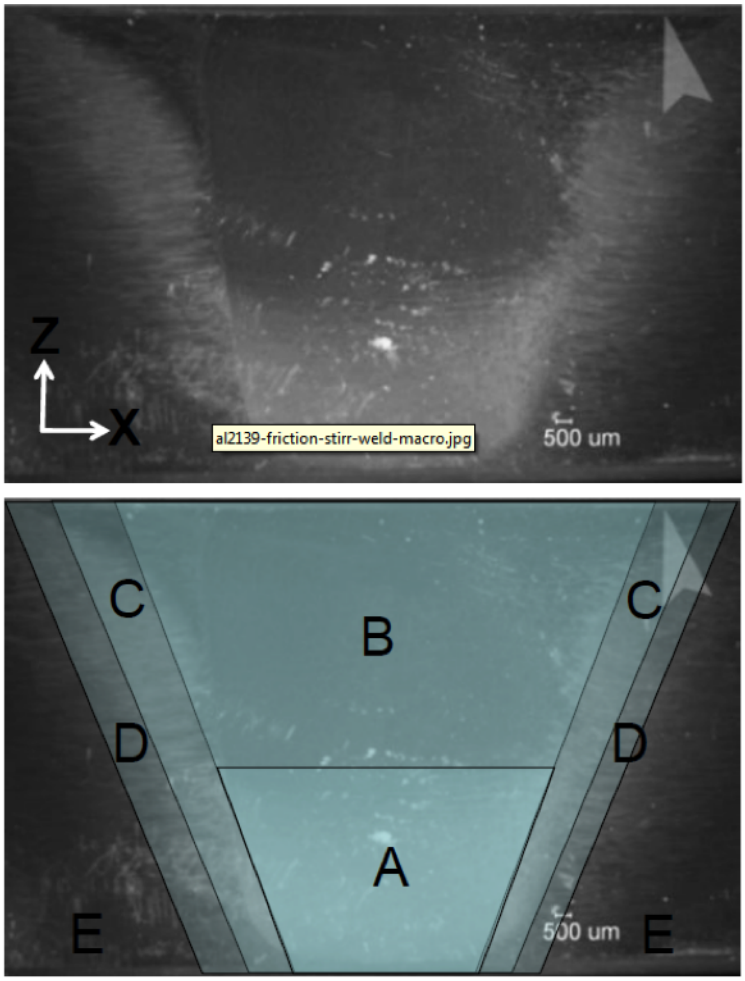

Figure 25: FSW Cross section for 2139 Aluminum. The labeled areas correspond to different weld zones which have distinct microstructural and mechanical properties. Zone A is the lower weld nugget, B the upper weld nugget, C the thermo-mechanical affected zone, and D the thermal affected zone.

the reduction at the strain rate 1E4 s^{-1}. This indicates that the effect of material inhomogeneity decreases with increasing strain rate. This is due to the fact that the material zones have the same rate hardening characteristics, which become increasingly prevalent relative to the inhomogeneous strain hardening characteristics as the applied strain rate increases.

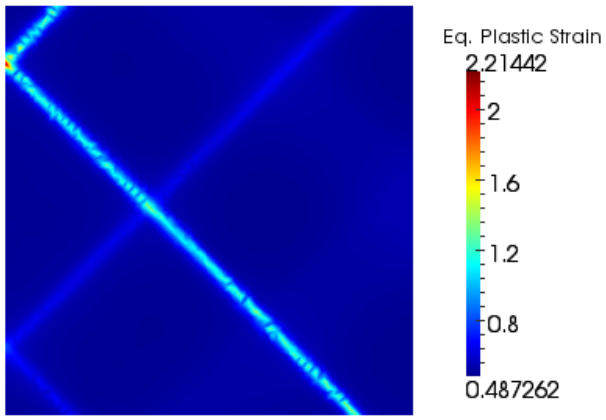

(a) Unaffected Aluminum at failure, Nominal Strain Rate 1E3

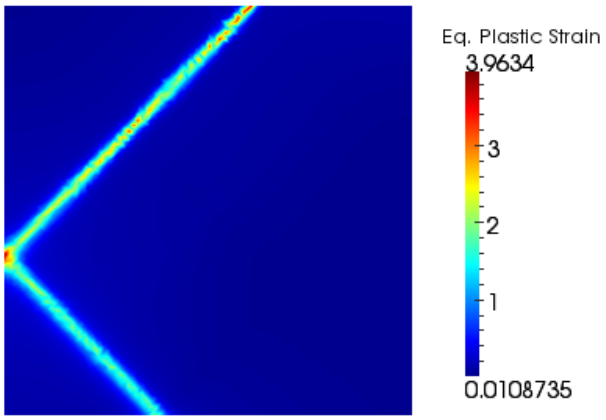

(b) Stir Weld at failure, Nominal Strain Rate 1E3

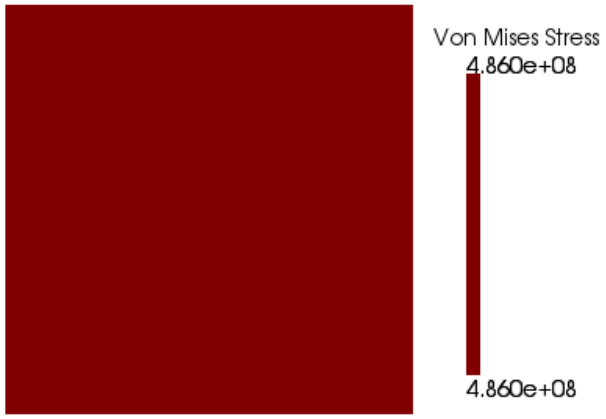

(c) Unaffected Aluminum at peak $\dot{\mathcal{W}}$, Nominal Strain Rate 1E3

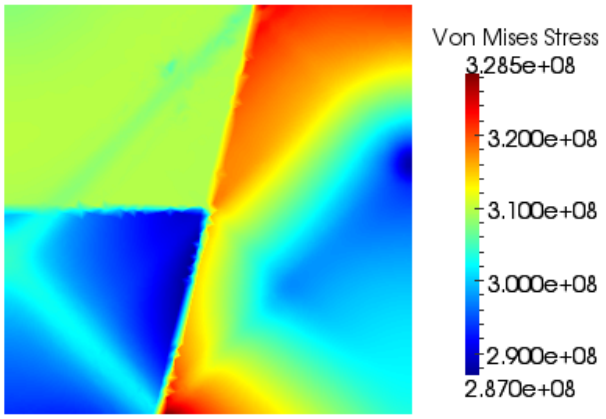

(d) Stir Weld at peak $\dot{\mathcal{W}}$, Nominal Strain Rate 1E3

Figure 26:

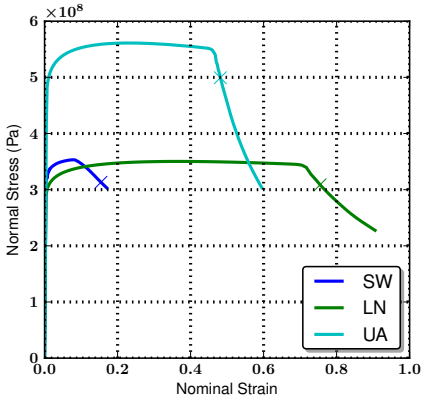

(a) Tensile Stress in the Direction of Loading, Nominal Strain Rate 1E3

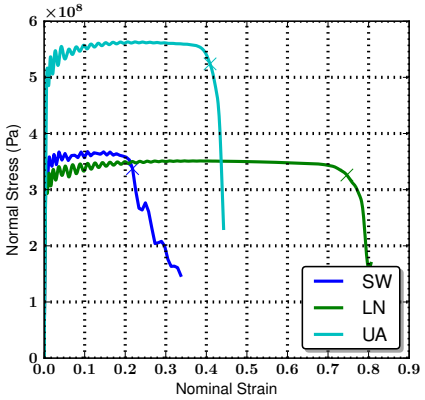

(b) Tensile Stress in the Direction of Loading, Nominal Strain Rate 1E4

Figure 27: Domain averaged tensile stress in the direction of loading vs nominal strain for each loading case. The x on the plot indicates the failure point.

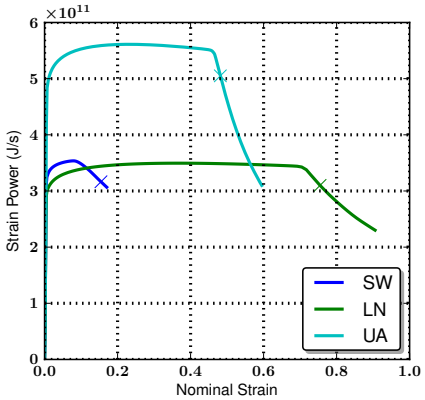

(a) $\dot{\mathcal{W}}$, Nominal Strain Rate 1E3

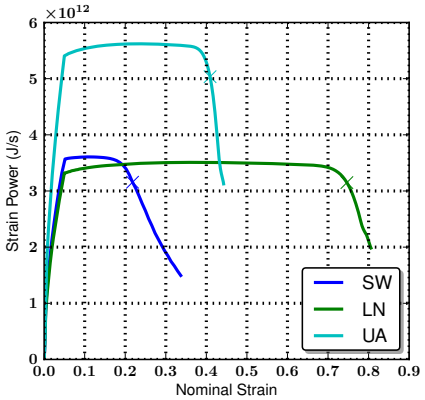

(b) $\dot{\mathcal{W}}$, Nominal Strain Rate 1E4

Figure 28: Rate of stress working for each case. The x on the plot indicate the failure point

Load Config. →	Cross Weld Tension		
Nom strain rate →	1E3		
Mat Config. ↓	Nom. Failure Strain	$\mathcal{W}$ at Failure	Failure Origin
UA	0.48	2.64e+08	N/A
LN	0.75	2.58e+08	N/A
SW	0.15	5.23e+07	UN-TMAZ Interface
Nom strain rate →	1E4		
Mat Config. ↓	Nom. Failure Strain	$\mathcal{W}$ at Failure	Failure Origin
UA	0.41	2.24e+08	N/A
LN	0.75	2.57e+08	N/A
SW	0.22	7.62e+07	UN-TMAZ Interface

Table 2: Results summary for the cross weld tension test: nominal strain at failure, $\mathcal{W}$ at failure, and failure initiation zone ae tabulated

4 Research Dissemination

Research Results were disseminated through conference presentations, invited seminars and keynote lectures, posters and refereed journal publications.

Resulting Journal Publications:

- Colin McAuliffe, Ryan Karkkainen, Chian Yen and Waisman, H. and Haim Waisman (2014), Numerical modeling of friction stir welded aluminum joints under high rate loading, Finite Elements in Analysis and Design 89:8-18.
- Colin McAuliffe and Haim Waisman (2015), A unified model for metal failure capturing shear banding and fracture, International Journal of Plasticity 65:131-151.
- Colin McAuliffe and Haim Waisman (2015), On the importance of nonlinear elastic effects in shear band modeling, International Journal of Plasticity 71:10-31.
- Colin McAuliffe and Haim Waisman (2016), A coupled phase field shear band model for Ductile-Brittle transition in notched plate impact, Computer Methods in Applied Mechanics and Engineering 305, 173-195, 2016.
- Miguel Arriaga and Haim Waisman (2017), Stability analysis of the phase-field method for fracture with a general degradation function and plasticity induced crack generation, Mechanics of Materials, http://dx.doi.org/10.1016/j.mechmat.2017.04.003 .
- Miguel Arriaga and Haim Waisman, Combined stability analysis of phase-field dynamic fracture and shear band localization (2017), International Journal of Plasticity 96:81-119.
- Miguel Arriaga and Haim Waisman (2017), A Multidimensional stability analysis of the phase-field method for fracture with a general degradation function and energy split, Computational Mechanics, DOI 10.1007/s00466-017-1432-1.

Invited Seminars and Keynote lectures (2016-2017) :

- Seminar: Dynamic Fracture of Metals, College of Mechanics of Materials, Hohai University, Nanjing, China, July 2017.
- Keynote Lecture: Stability analysis of the Phase Field method for fracture, United States National Congress on Computational Mechanics (USNCCM14), Montreal, Canada, Jul 2017.
- Invited Lecture: A unified model for metal failure capturing shear banding and fracture, IUTAM Symposium on Integrated Computational Structure-Material Modeling of Deformation & Failure Under Extreme Conditions, Baltimore, MD, Jun 2016.
- Keynote Lecture: Stability analysis of the Phase Field method for fracture, European Congress on Computational Methods in Applied Sciences and Engineering (ECCOMAS), Crete Island, Greece, Jun 2016.

- Invited Lecture: Towards stability analysis of a unified model for metal failure capturing shear banding and fracture", IUTAM Symposium on Dynamic Instabilities in Solids, Madrid, Spain, May 2016.

Conference presentations (2016-2017):

- An overlapping domain decomposition preconditioner for monolithic solution of shearbands, VII International Conference on Coupled problems in Science and Engineering, Rhodes Island, Greece, June 2017.
- Stability Analysis of Metals Capturing Brittle and Ductile Fracture through a Phase Field Method and Shear Band Localization, ASCE-Engineering Mechanics Institute conference, University of California San Diego, San Diego, CA, Jun 2017.
- Stability Analysis of Shear bands, ASCE-Engineering Mechanics Institute conference, Vanderbilt University, Nashville, TN, May 2016. (Presenter: Miguel Arriaga)
- Stability Analysis of Shear bands, Melosh Medal competition in Finite Element Analysis, Duke University, Durham, NC, April 2016. (Presenter: Miguel Arriaga)

5 Graduate Students Involved in the project

Two graduate students were funded by this project as listed below. Both students have graduated with a PhD degree and one student, Colin McAuliffe, continued to be supported by this project one more year as a postdoc. Furthermore, Colin McAuliffe had a successful internship with the Army Research Lab in Aberdeen Proving Ground, MD during summer of 2012.

Both students have presented their work in domestic and International conferences such as the ASCE-Engineering Mechanics Institute and US National Congress on Computational Mechanics. The two students were very successful in that their work was recognized by the community winning several awards in the field of computational mechanics. Furthermore, both students also won prestigious awards in the department for the best PhD thesis. Please see below a detailed award description.

- Colin McAuliffe (former Ph.D student and postdoc, now at Altair)
- Miguel Arriaga (former Ph.D student, now postdoc at Columbia University ME department)

6 Awards, Honors and Appointments

- Haim Waisman, elected chair of the Computational Mechanics committee in the Engineering Mechanics Institute of ASCE, September 2017.
- Haim Waisman, appointed associate editor of the journal of Engineering Mechanics, January 2017.
- Haim Waisman, Associate Professor received tenure at Columbia University, April 2016.

- Miguel Arriaga, won Second Place in Computational Mechanics Poster Competition at the EMI-ASCE Engineering Mechanics Institute conference at Vanderbilt University, Nashville, TN, May 2016.
- Miguel Arriaga, Awarded the Mindlin prize for the most outstanding PhD thesis in the Civil Engineering & Engineering Mechanics department at Columbia University, May 2016.
- Miguel Arriaga, Finalist Paper in the Robert J. Melosh competition for best paper on Finite Element Methods, Duke University, NC, April 2016.
- Miguel Arriaga, won Third Place in Computational Mechanics Poster Competition at the EMI-ASCE, McMaster University, Hamilton, Ontario, Canada, August 2014.
- Colin McAuliffe, Awarded the Mindlin prize for the most outstanding PhD thesis in the Civil Engineering & Engineering Mechanics department in Columbia University, May 2014.
- Haim Waisman, Awarded the EMI Leonardo Da Vinci Award (Young Investigator), ASCE-EMI institute, August 2014.

7 Bibliography

[1] D. Bigoni. Bifurcation and instability of non-associative elastoplastic solids. In *Material Instabilities in Elastic and Plastic Solids, Petryk H*, pages 1–52. Springer, 2000.

[2] A. Gajo, D. Bigoni, and D.Muir Wood. Multiple shear band development and related instabilities in granular materials. *Journal of the Mechanics and Physics of Solids*, 52(12): 2683–2724, 2004. ISSN 0022-5096. doi: 10.1016/j.jmps.2004.05.010.

[3] Y.L. Bai. Thermo-plastic instability in simple shear. *Journal of the Mechanics and Physics of Solids*, 30(4):195–207, 1982. ISSN 0022-5096. doi: 10.1016/0022-5096(82)90029-1.

[4] T.W. Wright and R.C. Batra. The initiation and growth of adiabatic shear bands. *International Journal of Plasticity*, 1(3):205–212, 1985. ISSN 0749-6419. doi: 10.1016/0749-6419(85)90003-8.

[5] T. W. Wright and J. W. Walter. On stress collapse in adiabatic shear bands. *Journal of the Mechanics and Physics of Solids*, 35(6):701–720, 1987. ISSN 0022-5096. doi: 10.1016/0022-5096(87)90051-2.

[6] Ioannis Tsagrakis and Elias C. Aifantis. On the Effect of Strain Gradient on Adiabatic Shear Banding. *Metallurgical and Materials Transactions A*, 46(10):4459–4467, 2014. ISSN 1073-5623, 1543-1940. doi: 10.1007/s11661-014-2586-5.

[7] T. W. Wright. *The Physics and Mathematics of Adiabatic Shear Bands*. Cambridge University Press, 2002.

[8] Benjamin Loret and Jean H. Prevost. Dynamic strain localization in elasto-(visco-)plastic solids, Part 1. General formulation and one-dimensional examples. *Computer Methods in Applied Mechanics and Engineering*, 83(3):247–273, 1990. ISSN 0045-7825. doi: 10.1016/0045-7825(90)90073-U.

[9] D. Rittel, P. Landau, and A. Venkert. Dynamic Recrystallization as a Potential Cause for Adiabatic Shear Failure. *Physical Review Letters*, 101(16):165501, 2008. doi: 10.1103/PhysRevLett.101.165501.

[10] H. M. Mourad, C. A. Bronkhorst, V. Livescu, J. N. Plohr, and E. K. Cerreta. Modeling and simulation framework for dynamic strain localization in elasto-viscoplastic metallic materials subject to large deformations. *International Journal of Plasticity*, 2016. ISSN 0749-6419. doi: 10.1016/j.ijplas.2016.09.009.

[11] S. Osovski, D. Rittel, and A. Venkert. The respective influence of microstructural and thermal softening on adiabatic shear localization. *Mechanics of Materials*, 56:11–22, 2013. ISSN 0167-6636. doi: 10.1016/j.mechmat.2012.09.008.

[12] A.G. Odeshi, M.N. Bassim, S. Al-Ameeri, and Q. Li. Dynamic shear band propagation and failure in AISI 4340 steel. *Journal of Materials Processing Technology*, 169(2):150–155, 2005. ISSN 0924-0136. doi: 10.1016/j.jmatprotec.2005.03.016.

[13] C. Fressengeas and A. Molinari. Instability and localization of plastic flow in shear at high strain rates. *Journal of the Mechanics and Physics of Solids*, 35(2):185–211, 1987. ISSN 0022-5096. doi: 10.1016/0022-5096(87)90035-4.

[14] Xianwu Ling and T. Belytschko. Thermal softening induced plastic instability in rate-dependent materials. *Journal of the Mechanics and Physics of Solids*, 57(4):788–802, 2009. ISSN 0022-5096. doi: 10.1016/j.jmps.2008.04.010.

[15] A. Marchand and J. Duffy. An experimental study of the formation process of adiabatic

shear bands in a structural steel. *Journal of the Mechanics and Physics of Solids*, 36(3): 251–283, 1988. ISSN 0022-5096. doi: 10.1016/0022-5096(88)90012-9.

[16] J. J. Mason, A. J. Rosakis, and G. Ravichandran. On the strain and strain rate dependence of the fraction of plastic work converted to heat: an experimental study using high speed infrared detectors and the Kolsky bar. *Mechanics of Materials*, 17(2–3):135–145, 1994. ISSN 0167-6636.

[17] P. Rosakis, A. J. Rosakis, G. Ravichandran, and J. Hodowany. A thermodynamic internal variable model for the partition of plastic work into heat and stored energy in metals. *Journal of the Mechanics and Physics of Solids*, 48(3):581 – 607, 2000. ISSN 0022-5096. doi: 10.1016/S0022-5096(99)00048-4.

[18] N. Aravas, K-S. Kim, and F. A. Leckie. On the Calculations of the Stored Energy of Cold Work. *Journal of Engineering Materials and Technology*, 112(4):465–470, 1990. ISSN 0094-4289. doi: 10.1115/1.2903358.

[19] M. Vural, G. Ravichandran, and D. Rittel. Large strain mechanical behavior of 1018 cold-rolled steel over a wide range of strain rates. *Metallurgical and Materials Transactions A*, 34(12):2873–2885, 2003. ISSN 1073-5623, 1543-1940. doi: 10.1007/s11661-003-0188-8.

[20] J. F. Kalthoff and S. Wrinkler. Failure mode transition at high rates of shear loading. *Impact Loading and Dynamic Behavior of Materials*, 1:185–195, 1987.

[21] M. Zhou, G. Ravichandran, and A.J. Rosakis. Dynamically propagating shear bands in impact-loaded prenotched plates-II. Numerical simulations. *Journal of the Mechanics and Physics of Solids*, 44(6):1007–1032, 1996. ISSN 0022-5096. doi: 10.1016/0022-5096(96)00004-X.

[22] Joerg F. Kalthoff. Modes of dynamic shear failure in solids. *International Journal of Fracture*, 101(1-2):1–31, 2000. ISSN 0376-9429, 1573-2673. doi: 10.1023/A:1007647800529.

[23] C. F. E. Tipper. *The brittle fracture story*. University Press, 1962.

[24] G H Nickodemus, L S Kramer, J R Pickens, and M S Burkins. Aluminum alloy. Advances for Ground Vehicles. *Advanced materials & processes*, 160(2):51–54, 2002. ISSN 0882-7958.

[25] Christian Miehe, Fadi Aldakheel, and Arun Raina. Phase field modeling of ductile fracture at finite strains: A variational gradient-extended plasticity-damage theory. *International Journal of Plasticity*, 84:1–32, 2016. ISSN 0749-6419. doi: 10.1016/j.ijplas.2016.04.011.

[26] Michael J. Borden, Thomas J. R. Hughes, Chad M. Landis, Amin Anvari, and Isaac J. Lee. A phase-field formulation for fracture in ductile materials: Finite deformation balance law derivation, plastic degradation, and stress triaxiality effects. *Computer Methods in Applied Mechanics and Engineering*, 2016. ISSN 0045-7825. doi: 10.1016/j.cma.2016.09.005.

[27] Colin McAuliffe and Haim Waisman. A unified model for metal failure capturing shear banding and fracture. *International Journal of Plasticity*, 65:131–151, 2015. ISSN 0749-6419. doi: 10.1016/j.ijplas.2014.08.016.

[28] Colin McAuliffe and Haim Waisman. A coupled phase field shear band model for ductile brittle transition in notched plate impacts. *Computer Methods in Applied Mechanics and Engineering*, 305:173–195, 2016. ISSN 0045-7825. doi: 10.1016/j.cma.2016.02.018.

[29] R. C. Batra and X. S. Jin. Analysis of dynamic shear bands in porous thermally softening viscoplatic materials. *Archives of Mechanics*, 46:13–36, 1994.

[30] Shaofan Li, Wing Kam Liu, Ares J. Rosakis, Ted Belytschko, and Wei Hao. Mesh-free Galerkin simulations of dynamic shear band propagation and failure mode transition. *Inter-*

national Journal of Solids and Structures, 39(5):1213–1240, 2002. ISSN 0020-7683. doi: 10.1016/S0020-7683(01)00188-3.

[31] F. Zhou, T. W. Wright, and K. T. Ramesh. The formation of multiple adiabatic shear bands. *Journal of the Mechanics and Physics of Solids*, 54(7):1376–1400, 2006. ISSN 0022-5096. doi: 10.1016/j.jmps.2006.01.006.

[32] C Beckermann, H. J Diepers, I Steinbach, A Karma, and X Tong. Modeling Melt Convection in Phase-Field Simulations of Solidification. *Journal of Computational Physics*, 154(2): 468–496, 1999. ISSN 0021-9991. doi: 10.1006/jcph.1999.6323.

[33] W. J. Boettinger, J. A. Warren, C. Beckermann, and A. Karma. Phase-Field Simulation of Solidification. *Annual Review of Materials Research*, 32(1):163–194, 2002. doi: 10.1146/annurev.matsci.32.101901.155803.

[34] Jun-Ho Jeong, Nigel Goldenfeld, and Jonathan A. Dantzig. Phase field model for three-dimensional dendritic growth with fluid flow. *Physical Review E*, 64(4):041602, 2001. doi: 10.1103/PhysRevE.64.041602.

[35] Y. H. Wen, Y. Wang, and L. Q. Chen. Phase-field simulation of domain structure evolution during a coherent hexagonal-to-orthorhombic transformation. *Philosophical Magazine A*, 80(9):1967–1982, 2000. ISSN 0141-8610. doi: 10.1080/01418610008212146.

[36] Mohsen Asle Zaeem and Sinisa Dj. Mesarovic. Finite element method for conserved phase fields: Stress-mediated diffusional phase transformation. *Journal of Computational Physics*, 229(24):9135–9149, 2010. ISSN 0021-9991. doi: 10.1016/j.jcp.2010.08.027.

[37] Y. Wang and A. G. Khachaturyan. Three-dimensional field model and computer modeling of martensitic transformations. *Acta Materialia*, 45(2):759–773, 1997. ISSN 1359-6454. doi: 10.1016/S1359-6454(96)00180-2.

[38] Mahmood Mamivand, Mohsen Asle Zaeem, and Haitham El Kadiri. A review on phase field modeling of martensitic phase transformation. *Computational Materials Science*, 77: 304–311, 2013. ISSN 0927-0256. doi: 10.1016/j.commatsci.2013.04.059.

[39] Y. U. Wang, Y. M. Jin, A. M. Cuitino, and A. G. Khachaturyan. Nanoscale phase field microelasticity theory of dislocations: model and 3d simulations. *Acta Materialia*, 49(10): 1847–1857, 2001. ISSN 1359-6454. doi: 10.1016/S1359-6454(01)00075-1.

[40] D. Fan and L. Q. Chen. Computer simulation of grain growth using a continuum field model. *Acta Materialia*, 45(2):611–622, 1997. ISSN 1359-6454. doi: 10.1016/S1359-6454(96)00200-5.

[41] A. Kazaryan, Y. Wang, S. A. Dregia, and Bruce R. Patton. Generalized phase-field model for computer simulation of grain growth in anisotropic systems. *Physical Review B*, 61(21): 14275–14278, 2000. doi: 10.1103/PhysRevB.61.14275.

[42] Hanen Amor, Jean-Jacques Marigo, and Corrado Maurini. Regularized formulation of the variational brittle fracture with unilateral contact: Numerical experiments. *Journal of the Mechanics and Physics of Solids*, 57(8):1209–1229, 2009. ISSN 0022-5096. doi: 10.1016/j.jmps.2009.04.011.

[43] Michael J. Borden, Clemens V. Verhoosel, Michael A. Scott, Thomas J. R. Hughes, and Chad M. Landis. A phase-field description of dynamic brittle fracture. *Computer Methods in Applied Mechanics and Engineering*, 217-220:77–95, 2012. ISSN 0045-7825. doi: 10.1016/j.cma.2012.01.008.

[44] B. Bourdin, G. A. Francfort, and J-J. Marigo. Numerical experiments in revisited brittle fracture. *Journal of the Mechanics and Physics of Solids*, 48(4):797–826, 2000. ISSN

0022-5096. doi: 10.1016/S0022-5096(99)00028-9.

[45] Fernando P. Duda, Angel Ciarbonetti, Pablo J. SÃ¡nchez, and Alfredo E. Huespe. A phase-field/gradient damage model for brittle fracture in elastic-plastic solids. *International Journal of Plasticity*, 65:269–296, 2015. ISSN 0749-6419. doi: 10.1016/j.ijplas.2014.09.005.

[46] Charlotte Kuhn and Ralf MÃŒller. Crack Nucleation in Phase Field Fracture Models. In *ICF13*, 2013.

[47] Stefan May, Julien Vignollet, and RenÃ© de Borst. A numerical assessment of phase-field models for brittle and cohesive fracture: Gamma-Convergence and stress oscillations. *European Journal of Mechanics - A/Solids*, 52:72–84, 2015. ISSN 0997-7538. doi: 10.1016/j.euromechsol.2015.02.002.

[48] Christian Miehe, Martina Hofacker, and Fabian Welschinger. A phase field model for rate-independent crack propagation: Robust algorithmic implementation based on operator splits. *Computer Methods in Applied Mechanics and Engineering*, 199(45-48):2765–2778, 2010. ISSN 0045-7825. doi: 10.1016/j.cma.2010.04.011.

[49] C. Miehe, F. Welschinger, and M. Hofacker. Thermodynamically consistent phase-field models of fracture: Variational principles and multi-field FE implementations. *International Journal for Numerical Methods in Engineering*, 83(10):1273–1311, 2010. ISSN 1097-0207. doi: 10.1002/nme.2861.

[50] Julien Vignollet, Stefan May, RenÃ© de Borst, and Clemens V. Verhoosel. Phase-field models for brittle and cohesive fracture. *Meccanica*, 49(11):2587–2601, 2014. ISSN 0025-6455, 1572-9648. doi: 10.1007/s11012-013-9862-0.

[51] Alain Karma and Alexander E. Lobkovsky. Unsteady Crack Motion and Branching in a Phase-Field Model of Brittle Fracture. *Physical Review Letters*, 92(24):245510, 2004. doi: 10.1103/PhysRevLett.92.245510.

[52] I. S. Aranson, V. A. Kalatsky, and V. M. Vinokur. Continuum Field Description of Crack Propagation. *Physical Review Letters*, 85(1):118–121, 2000. doi: 10.1103/PhysRevLett.85.118.

[53] Alain Karma, David A. Kessler, and Herbert Levine. Phase-Field Model of Mode III Dynamic Fracture. *Physical Review Letters*, 87(4), 2001. ISSN 0031-9007, 1079-7114. doi: 10.1103/PhysRevLett.87.045501. arXiv: cond-mat/0105034.

[54] L. O. Eastgate, J. P. Sethna, M. Rauscher, T. Cretegny, C.-S. Chen, and C. R. Myers. Fracture in mode I using a conserved phase-field model. *Physical Review. E, Statistical, Nonlinear, and Soft Matter Physics*, 65(3 Pt 2A):036117, 2002. ISSN 1539-3755. doi: 10.1103/PhysRevE.65.036117.

[55] Markus Klinsmann, Daniele Rosato, Marc Kamlah, and Robert M. McMeeking. An assessment of the phase field formulation for crack growth. *Computer Methods in Applied Mechanics and Engineering*, 294:313–330, 2015. ISSN 0045-7825. doi: 10.1016/j.cma.2015.06.009.

[56] Kim Pham and Jean-Jacques Marigo. From the onset of damage to rupture: construction of responses with damage localization for a general class of gradient damage models. *Continuum Mechanics and Thermodynamics*, 25(2-4):147–171, 2011. ISSN 0935-1175, 1432-0959. doi: 10.1007/s00161-011-0228-3.

[57] Charlotte Kuhn, Alexander SchlÃŒter, and Ralf MÃŒller. On degradation functions in phase field fracture models. *Computational Materials Science*, 108, Part B:374–384, 2015. ISSN 0927-0256. doi: 10.1016/j.commatsci.2015.05.034.

[58] Michael Johns Borden. *Isogeometric analysis of phase-field models for dynamic brittle and ductile fracture*. thesis, University of Texas at Austin, 2012.

[59] M. Zhou, A.J. Rosakis, and G. Ravichandran. Dynamically propagating shear bands in impact-loaded prenotched plates-I. Experimental investigations of temperature signatures and propagation speed. *Journal of the Mechanics and Physics of Solids*, 44(6):981–1006, 1996. ISSN 0022-5096. doi: 10.1016/0022-5096(96)00003-8.

[60] M. Zhou, A. Needleman, and R.J. Clifton. Finite element simulations of shear localization in plate impact. *Journal of the Mechanics and Physics of Solids*, 42(3):423–458, 1994. ISSN 0022-5096. doi: 10.1016/0022-5096(94)90026-4.

[61] Ted Belytschko, Huai-Yang Chiang, and Edward Plaskacz. High resolution two-dimensional shear band computations: imperfections and mesh dependence. *Computer Methods in Applied Mechanics and Engineering*, 119(1-2):1–15, 1994. ISSN 0045-7825. doi: 10.1016/0045-7825(94)00073-5.

[62] R.C. Batra. The initiation and growth of, and the interaction among, adiabatic shear bands in simple and dipolar materials. *International Journal of Plasticity*, 3(1):75–89, 1987. ISSN 0749-6419. doi: 10.1016/0749-6419(87)90019-2.

[63] R.C. Batra and L. Chen. Effect of viscoplastic relations on the instability strain, shear band initiation strain, the strain corresponding to the minimum shear band spacing, and the band width in a thermoviscoplastic material. *International Journal of Plasticity*, 17(11):1465–1489, 2001. ISSN 0749-6419. doi: 10.1016/S0749-6419(01)00004-3.

[64] E. C. Aifantis. On the Microstructural Origin of Certain Inelastic Models. *Journal of Engineering Materials and Technology*, 106(4):326–330, 1984. ISSN 0094-4289. doi: 10.1115/1.3225725.

[65] Elias C. Aifantis. The physics of plastic deformation. *International Journal of Plasticity*, 3 (3):211–247, 1987. ISSN 0749-6419. doi: 10.1016/0749-6419(87)90021-0.

[66] Rashid K. Abu Al-Rub and George Z. Voyiadjis. A physically based gradient plasticity theory. *International Journal of Plasticity*, 22(4):654–684, 2006. ISSN 0749-6419. doi: 10.1016/j.ijplas.2005.04.010.

[67] Rashid K. Abu Al-Rub and George Z. Voyiadjis. A Finite Strain Plastic-damage Model for High Velocity Impact using Combined Viscosity and Gradient Localization Limiters: Part I - Theoretical Formulation. *International Journal of Damage Mechanics*, 15(4):293–334, 2006. ISSN 1056-7895, 1530-7921. doi: 10.1177/1056789506058046.

[68] George Z. Voyiadjis and Rashid K. Abu Al-Rub. A Finite Strain Plastic-damage Model for High Velocity Impacts using Combined Viscosity and Gradient Localization Limiters: Part II - Numerical Aspects and Simulations. *International Journal of Damage Mechanics*, 15 (4):335–373, 2006. ISSN 1056-7895, 1530-7921. doi: 10.1177/1056789506058047.

[69] E. N. Lages, G. H. Paulino, I. F. M. Menezes, and R. R. Silva. Nonlinear Finite Element Analysis using an Object-Oriented Philosophy - Application to Beam Elements and to the Cosserat Continuum. *Engineering with Computers*, 15(1):73–89, 1999. ISSN 0177-0667, 1435-5663. doi: 10.1007/s003660050006.

[70] A. Cemal Eringen. *Nonlocal Continuum Field Theories*. Springer New York, 2002. ISBN 978-0-387-95275-8.

[71] Zdenek P BaÅŸant and Milan JirÃ¡sek. Nonlocal integral formulations of plasticity and damage: survey of progress. *Journal of Engineering Mechanics*, 128(11):1119–1149, 2002.

[72] R.H.J. Peerlings, M.G.D. Geers, R. de Borst, and W.A.M. Brekelmans. A critical com-

parison of nonlocal and gradient-enhanced softening continua. *International Journal of Solids and Structures*, 38(44-45):7723–7746, 2001. ISSN 0020-7683. doi: 10.1016/S0020-7683(01)00087-7.

[73] Shaofan Li, Wei Hao, and Wing Kam Liu. Mesh-free simulations of shear banding in large deformation. *International Journal of Solids and Structures*, 37(48-50):7185–7206, 2000. ISSN 0020-7683. doi: 10.1016/S0020-7683(00)00195-5.

[74] Shaofan Li and Wing Kam Liu. Numerical simulations of strain localization in inelastic solids using mesh-free methods. *International Journal for Numerical Methods in Engineering*, 48(9):1285–1309, 2000.

[75] Luc Berger-Vergiat, Colin McAuliffe, and Haim Waisman. Isogeometric analysis of shear bands. *Computational Mechanics*, 54(2):503–521, 2014. ISSN 0178-7675. doi: 10.1007/s00466-014-1002-8.

[76] George Z. Voyiadjis and Navid Mozaffari. Nonlocal damage model using the phase field method: Theory and applications. *International Journal of Solids and Structures*, 50(20-21): 3136–3151, 2013. ISSN 0020-7683. doi: 10.1016/j.ijsolstr.2013.05.015.

[77] R. de Borst and C. V. Verhoosel. Gradient damage vs phase-field approaches for fracture: Similarities and differences. *Computer Methods in Applied Mechanics and Engineering*, 2016. ISSN 0045-7825. doi: 10.1016/j.cma.2016.05.015.

[78] Blaise Bourdin, Christopher J. Larsen, and Casey L. Richardson. A time-discrete model for dynamic fracture based on crack regularization. *International Journal of Fracture*, 168(2): 133–143, 2010. ISSN 0376-9429, 1573-2673. doi: 10.1007/s10704-010-9562-x.

[79] M. Ambati, T. Gerasimov, and L. De Lorenzis. Phase-field modeling of ductile fracture. *Computational Mechanics*, 55(5):1017–1040, 2015. ISSN 0178-7675, 1432-0924. doi: 10.1007/s00466-015-1151-4.

[80] Christian Miehe, Lisa-Marie Schanzel, and Heike Ulmer. Phase field modeling of fracture in multi-physics problems. Part I. Balance of crack surface and failure criteria for brittle crack propagation in thermo-elastic solids. *Computer Methods in Applied Mechanics and Engineering*, 294:449–485, 2015. ISSN 0045-7825. doi: 10.1016/j.cma.2014.11.016.

[81] Colin McAuliffe and Haim Waisman. Mesh insensitive formulation for initiation and growth of shear bands using mixed finite elements. *Computational Mechanics*, 51(5):807–823, 2013. ISSN 0178-7675, 1432-0924. doi: 10.1007/s00466-012-0765-z.

[82] Colin McAuliffe and Haim Waisman. A Pian-Sumihara type element for modeling shear bands at finite deformation. *Computational Mechanics*, 53(5):925–940, 2014. ISSN 0178-7675, 1432-0924. doi: 10.1007/s00466-013-0940-x.

[83] C. Miehe, M. Hofacker, L. M. Schanzel, and F. Aldakheel. Phase field modeling of fracture in multi-physics problems. Part II. Coupled brittle-to-ductile failure criteria and crack propagation in thermo-elastic-plastic solids. *Computer Methods in Applied Mechanics and Engineering*, 294:486–522, 2015. ISSN 0045-7825. doi: 10.1016/j.cma.2014.11.017.

[84] R. De Borst. Bifurcations in finite element models with a non-associated flow law. *International Journal for Numerical and Analytical Methods in Geomechanics*, 12(1):99–116, 1988. ISSN 1096-9853. doi: 10.1002/nag.1610120107.

[85] A. Needleman. Non-normality and bifurcation in plane strain tension and compression. *Journal of the Mechanics and Physics of Solids*, 27(3):231 – 254, 1979. ISSN 0022-5096. doi: http://dx.doi.org/10.1016/0022-5096(79)90003-6.

[86] R. de Borst. Computation of post-bifurcation and post-failure behavior of strain-

softening solids. *Computers & Structures*, 25(2):211–224, 1987. ISSN 0045-7949. doi: 10.1016/0045-7949(87)90144-1.

[87] Kim Pham, Hanen Amor, Jean-Jacques Marigo, and Corrado Maurini. Gradient Damage Models and Their Use to Approximate Brittle Fracture. *International Journal of Damage Mechanics*, 20(4):618–652, 2011. ISSN 1056-7895, 1530-7921. doi: 10.1177/1056789510386852.

[88] Miguel Arriaga, Colin McAuliffe, and Haim Waisman. Onset of shear band localization by a local generalized eigenvalue analysis. *Computer Methods in Applied Mechanics and Engineering*, 289:179–208, 2015. ISSN 0045-7825. doi: 10.1016/j.cma.2015.02.010.

[89] Miguel Arriaga, Colin McAuliffe, and Haim Waisman. Instability analysis of shear bands using the instantaneous growth-rate method. *International Journal of Impact Engineering*, 87:156–168, 2016. ISSN 0734-743X. doi: 10.1016/j.ijimpeng.2015.04.004.

[90] T. Rabczuk, P. M. A. Areias, and T. Belytschko. A simplified mesh-free method for shear bands with cohesive surfaces. *International Journal for Numerical Methods in Engineering*, 69(5):993–1021, 2007. ISSN 1097-0207. doi: 10.1002/nme.1797.

[91] Jeong-Hoon Song, Pedro M. A. Areias, and Ted Belytschko. A method for dynamic crack and shear band propagation with phantom nodes. *International Journal for Numerical Methods in Engineering*, 67(6):868–893, 2006. ISSN 1097-0207. doi: 10.1002/nme.1652.

[92] Ted Belytschko, Stefan Loehnert, and Jeong-Hoon Song. Multiscale aggregating discontinuities: A method for circumventing loss of material stability. *International Journal for Numerical Methods in Engineering*, 73(6):869–894, 2008. ISSN 1097-0207. doi: 10.1002/nme.2156.

[93] Alireza Tabarraei, Jeong-Hoon Song, and Haim Waisman. A Two-scale Strong Discontinuity Approach For Evolution Of Shear Bands Under Dynamic Impact Loads. *International Journal for Multiscale Computational Engineering*, 11(6):543–563, 2013. ISSN 1543-1649. doi: 10.1615/IntJMultCompEng.2013005506.

[94] T. Rabczuk and E. Samaniego. Discontinuous modelling of shear bands using adaptive meshfree methods. *Computer Methods in Applied Mechanics and Engineering*, 197(6-8): 641–658, 2008. ISSN 0045-7825. doi: 10.1016/j.cma.2007.08.027.

[95] Ted Belytschko, Hao Chen, Jingxiao Xu, and Goangseup Zi. Dynamic crack propagation based on loss of hyperbolicity and a new discontinuous enrichment. *International Journal for Numerical Methods in Engineering*, 58(12):1873–1905, 2003. ISSN 1097-0207. doi: 10.1002/nme.941.

[96] L. Anand, K.H. Kim, and T.G. Shawki. Onset of shear localization in viscoplastic solids. *Journal of the Mechanics and Physics of Solids*, 35(4):407–429, 1987. ISSN 0022-5096. doi: 10.1016/0022-5096(87)90045-7.

[97] R.C. Batra and Z.G. Wei. Instability strain and shear band spacing in simple tensile/compressive deformations of thermoviscoplastic materials. *International Journal of Impact Engineering*, 34(3):448–463, 2007. ISSN 0734-743X. doi: 10.1016/j.ijimpeng.2005.11.004.

[98] L.H. Dai and Y.L. Bai. Basic mechanical behaviors and mechanics of shear banding in BMGs. *International Journal of Impact Engineering*, 35(8):704–716, 2008. ISSN 0734-743X. doi: 10.1016/j.ijimpeng.2007.10.007.

[99] Jwo Pan. Perturbation analysis of shear strain localization in rate sensitive materials. *International Journal of Solids and Structures*, 19(2):153–164, 1983. ISSN 0020-7683. doi:

10.1016/0020-7683(83)90006-9.

[100] T.W. Wright. Shear band susceptibility: Work hardening materials. *International Journal of Plasticity*, 8(5):583–602, 1992. ISSN 0749-6419. doi: 10.1016/0749-6419(92)90032-8.

[101] J. N. Baucom and M. A. Zikry. Perturbation analysis of high strain-rate shear localization in B.C.C. crystalline materials. *Acta Mechanica*, 137(1-2):109–129, 1999. ISSN 0001-5970, 1619-6937. doi: 10.1007/BF01313148.

[102] Kwon Hee Kim. *Shear Localization in Viscoplastic Solids*. Ph.D. Dissertation, Department of Mechanical Engineering, Massachusetts Institute of Technology, 1987.

[103] D Bigoni and D Zaccaria. On the eigenvalues of the acoustic tensor in elastoplasticity. *Eur. J. Mech., A/Solids*, 13(5):621–638, 1994.

[104] Ronaldo I. Borja. Bifurcation of elastoplastic solids to shear band mode at finite strain. *Computer Methods in Applied Mechanics and Engineering*, 191(46):5287–5314, 2002. ISSN 0045-7825. doi: 10.1016/S0045-7825(02)00459-0.

[105] L. Szabo. On the Eigenvalues of the Fourth-Order Constitutive Tensor and Loss of Strong Ellipticity in Elastoplasticity. *International Journal of Plasticity*, 13(10):809–835, 1997. ISSN 0749-6419. doi: 10.1016/S0749-6419(97)00067-3.

[106] Liang Xue and Ted Belytschko. Fast methods for determining instabilities of elastic-plastic damage models through closed-form expressions. *International Journal for Numerical Methods in Engineering*, 84(12):1490–1518, 2010. ISSN 1097-0207. doi: 10.1002/nme.2947.

[107] J. Lemonds and A. Needleman. Finite element analyses of shear localization in rate and temperature dependent solids. *Mechanics of Materials*, 5(4):339–361, 1986. ISSN 0167-6636. doi: 10.1016/0167-6636(86)90039-6.

[108] A. Needleman. Material rate dependence and mesh sensitivity in localization problems. *Computer Methods in Applied Mechanics and Engineering*, 67(1):69–85, 1988. ISSN 0045-7825. doi: 10.1016/0045-7825(88)90069-2.

[109] E. A. Burroughs, L. A. Romero, R. B. Lehoucq, and A. G. Salinger. Large Scale Eigenvalue Calculations for Computing the Stability of Buoyancy Driven Flows. Technical report, Sandia National Laboratories, Albuquerque N.M., 2001.

[110] H. Mittelmann, K. Chang, and D. Jankowski. Iterative Solution of the Eigenvalue Problem in Hopf Bifurcation for the Boussinesq Equations. *SIAM Journal on Scientific Computing*, 15(3):704–712, 1994. ISSN 1064-8275. doi: 10.1137/0915045.

[111] Brian F. Farrell and Petros J. Ioannou. Generalized Stability Theory. Part I: Autonomous Operators. *Journal of the Atmospheric Sciences*, 53(14):2025–2040, 1996. ISSN 0022-4928. doi: 10.1175/1520-0469(1996)053<2025:GSTPIA>2.0.CO;2.

[112] Brian F. Farrell and Petros J. Ioannou. Generalized Stability Theory. Part II: Nonautonomous Operators. *Journal of the Atmospheric Sciences*, 53(14):2041–2053, 1996. ISSN 0022-4928. doi: 10.1175/1520-0469(1996)053<2041:GSTPIN>2.0.CO;2.

[113] C. McAuliffe and H. Waisman. A unified model for metal failure capturing shear banding and fracture. *International Journal of Plasticity*, 65:131–151, 2015.

[114] Colin McAuliffe and Haim Waisman. On the importance of nonlinear elastic effects in shear band modeling. *International Journal of Plasticity*, 71:10–31, 2015. ISSN 0749-6419. doi: 10.1016/j.ijplas.2015.04.004.

[115] M. Arriaga and H. Waisman. Multidimensional stability analysis of the phase-field method for fracture with a general degradation function and energy split. *Comp Mech*, in press,

2017.

[116] M. Arriaga and H. Waisman. Combined stability analysis of phase-field dynamic fracture and shear band localization. *Int J Plast*, 96:81–119, 2017.

[117] M. Arriaga and H. Waisman. Stability analysis of the phase-field method for fracture with a general degradation function and plasticity induced crack generation. *Mech Mat*, in press, 2017.

[118] C. McAuliffe, R. Karkkainen, C. Yen, and H. Waisman. Numerical modeling of friction stir welded aluminum joints under high rate loading. *Finite Elements in Analysis and Design*, 89:8–18, October 2014. ISSN 0168-874X. doi: 10.1016/j.finel.2014.04.012.

[119] C. McAuliffe and H. Waisman. A coupled phase field shear band model for Ductile-Brittle transition in notched plate impacts. *Computer Methods in Applied Mechanics and Engineering*, 305:173–195, 2016.

[120] C. McAuliffe and H. Waisman. On the importance of nonlinear elastic effects in shear band modeling. *International Journal of Plasticity*, 71:10–31, 2015.

[121] J.C. Simo and T.J.R Hughes. *Computational Inelasticity*. Springer, Springer, New York, 1998. ISBN 0387227636.

[122] T.W. Wright and J.W. Walter. On stress collapse in adiabatic shear bands. *Journal of the Mechanics and Physics of Solids*, 35(6):701 – 720, 1987. ISSN 0022-5096. doi: http://dx.doi.org/10.1016/0022-5096(87)90051-2. URL `http://www.sciencedirect.com/science/article/pii/0022509687900512`.

[123] T.W. Wright. *The Physics and Mathematics of Adiabatic Shear Bands*. Cambridge University Press, 2002.

[124] C. McAuliffe and H. Waisman. Mesh insensitive formulation for initiation and growth of shear bands using mixed finite elements. *Computational Mechanics*, 51(5):807–823, May 2013. ISSN 0178-7675, 1432-0924. doi: 10.1007/s00466-012-0765-z.

[125] C. McAuliffe and H. Waisman. A Pian–Sumihara type element for modeling shear bands at finite deformation. *Computational Mechanics*, 53(5):925–940, May 2014. ISSN 0178-7675, 1432-0924. doi: 10.1007/s00466-013-0940-x.

[126] L. Berger-Vergiat, C. McAuliffe, and H. Waisman. Isogeometric analysis of shear bands. *Computational Mechanics*, 54(2):503–521, August 2014. ISSN 0178-7675, 1432-0924. doi: 10.1007/s00466-014-1002-8.

[127] M. J. Borden, C. V. Verhoosel, M. A. Scott, T.J.R. Hughes, and C. M. Landis. A phase-field description of dynamic brittle fracture. *Computer Methods in Applied Mechanics and Engineering*, 217:77–95, 2012.

[128] C. Miehe, F. Welschinger, and M. Hofacker. Thermodynamically consistent phase-field models of fracture: Variational principles and multi-field FE implementations. *International Journal for Numerical Methods in Engineering*, 83(10):1273–1311, 2010.

[129] C. Miehe, M. Hofacker, and F. Welschinger. A phase field model for rate-independent crack propagation: Robust algorithmic implementation based on operator splits. *Computer Methods in Applied Mechanics and Engineering*, 199(45):2765–2778, 2010.

[130] R. de Borst, J. Pamin, R.H.J. Peerlings, and L.J. Sluys. On gradient-enhanced damage and plasticity models for failure in quasi-brittle and frictional materials. *Computational Mechanics*, 17:130–141, 1995.

[131] A. L. Gurson. *Plastic flow and fracture behavior of ductile materials, incorporating void nucleation, growth, and interaction*. PhD thesis, Brown University Providence, RI, 1975.

[132] V. Tvergaard and A. Needleman. Analysis of the cup-cone fracture in a round tensile bar. *Acta Metallurgica*, 32(1):157–169, 1984.

[133] I. Babuska. Error Bounds for Finite Element Method. *Numerische Mathematik*, 16:322–333, 1971.

[134] F. Brezzi. On the existence, uniqueness and approximation of saddle-point problems arising from Lagrangian multipliers. *Rev. Francaise Automat. Informat. Recherche Opérationnelle Sér. Rouge*, 8:129–151, 1974.

[135] L. Berger-Vergiat, C. McAuliffe, and H. Waisman. Parallel preconditioners for monolithic solution of shearbands. *Journal of Computational Physics*, 304:359–379, 2016.

[136] J. F. Kalthoff and S. Winkler. Failure mode transition at high rates of shear loading. In C. Chiem, H. D. Kunze, and L. W. Meyer, editors, *Impact Loading and Dynamic Behavior of Materials, vol. 1*, pages 185–195. DGM Informationsgesellschaft Verlag, 1987.

[137] J. F. Kalthoff. Modes of dynamic shear failure in solids. *International Journal of fracture*, 101:1–31, 2000.

[138] Edward John Routh. *A Treatise on the Stability of a Given State of Motion: Particularly Steady Motion*. Macmillan and Company, 1877.

[139] A. Hurwitz. Ueber die Bedingungen, unter welchen eine Gleichung nur Wurzeln mit negativen reellen Theilen besitzt. *Mathematische Annalen*, 46:273–284, 1895. ISSN 0025-5831; 1432-1807.

[140] Y. Leroy and M. Ortiz. Finite element analysis of transient strain localization phenomena in frictional solids. *International Journal for Numerical and Analytical Methods in Geomechanics*, 14(2):93–124, 1990. ISSN 1096-9853. doi: 10.1002/nag.1610140203.

[141] Prof Ivo BabuÅ¡ka. Error-bounds for finite element method. *Numerische Mathematik*, 16 (4):322–333, 1971. ISSN 0029-599X, 0945-3245. doi: 10.1007/BF02165003.

[142] F. Brezzi. On the existence, uniqueness and approximation of saddle-point problems arising from lagrangian multipliers. *ESAIM: Mathematical Modelling and Numerical Analysis - ModÃ©lisation MathÃ©matique et Analyse NumÃ©rique*, 8(R2):129–151, 1974.

[143] E. Reissner. On a variational theorem in elasticity. *Journal of Mathematical Physics*, 29(2): 90–95, 1950.

[144] Gordon R. Johnson and William H. Cook. Fracture characteristics of three metals subjected to various strains, strain rates, temperatures and pressures. *Engineering Fracture Mechanics*, 21(1):31 – 48, 1985. ISSN 0013-7944. doi: http://dx.doi.org/10.1016/0013-7944(85)90052-9.

[145] Jorg F. Kalthoff. Shadow Optical Analysis Of Dynamic Shear Fracture. *Optical Engineering*, 27(10):835–840, 1988. ISSN 0091-3286. doi: 10.1117/12.7976772.

[146] Pedro M. A. Areias and Ted Belytschko. Two-scale shear band evolution by local partition of unity. *International Journal for Numerical Methods in Engineering*, 66(5):878–910, 2006. ISSN 1097-0207. doi: 10.1002/nme.1589.

[147] Pedro M. A. Areias and Ted Belytschko. Two-scale method for shear bands: thermal effects and variable bandwidth. *International Journal for Numerical Methods in Engineering*, 72 (6):658–696, 2007. ISSN 1097-0207. doi: 10.1002/nme.2028.

[148] C. J. Dawes and W. M. Thomas. Friction stir process welds alluminum alloys. *Welding Journal*, 75:41–52, 1996.

[149] W. M. Thomas, E. D. Nicholas, J. C. Needham, M. G. Murch, P. Temple-Smith, and C. J. Dawes. Friction stir butt welding. (Internaional Patent Number PCT/GB92/02203), 1991.

[150] W. M. Thomas and R. E. Dolby. Friction stir process welds alluminum alloys. In S. A. David, T. DebRoy, J. C. Lippold, H. B. Smartt, and J. M. Vitek, editors, *Proceedings of the Sixth International Conference on Trends in Welding Research*. ASM International, Materials Park, Ohio, 1996.

[151] W. M. Thomas and E. D. Nicholas. Friction stir welding for the transporation industries. *Material Design*, 18:267–273, 1997.

[152] K. V. Jata and S. L. Semiatin. Continuous dynamic recrystallization during friction stir welding of high strength aluminum alloys. *Scripta Materialia*, 43(8):743–749, September 2000. ISSN 1359–6462. doi: 10.1016/S1359-6462(00)00480-2. URL http://www.sciencedirect.com/science/article/pii/S1359646200004802.

[153] Beate Heinz and Birgit Skrotzki. Characterization of a friction-stir-welded aluminum alloy 6013. *Metallurgical and Materials Transactions B*, 33(3):489–498, June 2002. ISSN 1073-5615, 1543-1916. doi: 10.1007/s11663-002-0059-5. URL http://link.springer.com/article/10.1007/s11663-002-0059-5.

[154] H. Liu, H. Fulii, M. Maeda, and K. Nogi. Tensile properties and fracture locations of friction-stir welded joints of 6061-t6 aluminium alloy. *Journal of Material Science Letters*, 22:1061–1063, 2003.

[155] J. Q. Su, T. W. Nelson, R. Mishra, and M. Mahoney. Microstructural investigation of friction stir welded 7050-t651 aluminum. *Acta Mater*, 51:713–729, 2003.

[156] Influence of friction stir welding parameters on grain size and formability in 5083 aluminum alloy. 456. ISSN 0921–5093.

[157] H. Schmidt, J. Hattel, and J. Wert. An analytical model for the heat generation in friction stir welding. *Modelling and Simulation in Materials Science and Engineering*, 12 (1):143, January 2004. ISSN 0965–0393. doi: 10.1088/0965-0393/12/1/013. URL http://iopscience.iop.org/0965-0393/12/1/013.

[158] Brian Justusson. Microstructural Investigation and Evaluation of Mechanical Properties in Friction Stir Welded Joints. Technical Report ADA558384, U. S. Army Research Labortory WMRD RDRL-WMM-B, Aberdeen Proving Ground, MD, 21005, 2011.

[159] Brian Justusson, Jessica Medintz, Jian Yu, Constantine Fountzoulas, and Chian Fong Yen. Spatial Mechanical Response and Strain Gradient Evolution of Friction Stir Welded Aluminum-2139. Technical Report ARL-TR-5892, U.S. Army Research Laboratory RDRL-WMM-B, Aberdeen Proving Ground, MD 21005, 2012.

[160] G. Buffa, L. Fratini, and R. Shivpuri. CDRX modelling in friction stir welding of AA7075-T6 aluminum alloy: Analytical approaches. *Journal of Materials Processing Technology*, 191(1–3):356–359, August 2007. ISSN 0924–0136. doi: 10.1016/j.jmatprotec.2007.03.033. URL http://www.sciencedirect.com/science/article/pii/S0924013607002671.

[161] Livan Fratini and Gianluca Buffa. CDRX modelling in friction stir welding of aluminium alloys. *International Journal of Machine Tools and Manufacture*, 45(10): 1188–1194, August 2005. ISSN 0890-6955. doi: 10.1016/j.ijmachtools.2004.12.001. URL http://www.sciencedirect.com/science/article/pii/S0890695504003189.

[162] Livan Fratini, Gianluca Buffa, and Dina Palmeri. Using a neural network for predicting the average grain size in friction stir welding processes. *Computers & Structures*, 87(17–18):1166–1174, September 2009. ISSN 0045–7949. doi: 10.1016/j.compstruc.2009.04.008. URL

http://www.sciencedirect.com/science/article/pii/S0045794909001370.

[163] M. Grujicic, T. He, G. Arakere, H. V. Yalavarthy, C. F. Yen, and B. A. Cheeseman. Fully coupled thermomechanical finite element analysis of material evolution during friction stir welding of aa5083. *Journal of Engineering Manufacture*, 224:609–625, 2009.

[164] M. Grujicic, G. Arakere, P. Pandurangan, C. F. Yen, B. A. Cheeseman, A. P. Reynolds, and M. A. Sutton. Computational analysis of material flow during friction stir welding of aa5059 aluminum alloys. *Journal Materials Engineering and Performance*, 21:1824–1840, 2012.

[165] M. Grujicic, P. Pandurangan, C. F. Yen, and B. A. Cheeseman. Modifications in the aa5083 johnson-cook material model for use in friction stir welding computational analyses. *Journal Materials Engineering and Performance*, 21:2207–2217, 2012.

[166] C. M. Chen and R. Kovacevic. Finite element modeling of friction stir welding-thermal and thermomechanical analysis. *International Journal of Machine Tools and Manufacture*, 43(13):1319–1326, October 2003. ISSN 0890-6955. doi: 10.1016/S0890-6955(03)00158-5. URL http://www.sciencedirect.com/science/article/pii/S0890695503001585.

[167] H. W. Zhang, Z. Zhang, and J. T. Chen. The finite element simulation of the friction stir welding process. *Materials Science and Engineering: A*, 403(1–2): 340–348, August 2005. ISSN 0921–5093. doi: 10.1016/j.msea.2005.05.052. URL http://www.sciencedirect.com/science/article/pii/S0921509305005472.

[168] D. Jacquin, B. de Meester, A. Simar, D. Deloison, F. Montheillet, and C. Desrayaud. A simple eulerian thermomechanical modeling of friction stir welding. *Journal of Materials Processing Technology*, 211(1):57–65, January 2011. ISSN 0924–0136. doi: 10.1016/j.jmatprotec.2010.08.016. URL http://www.sciencedirect.com/science/article/pii/S092401361000258X.

[169] A. Marchand and J. Duffy. An experimental study of the formation process of adiabatic shear bands. *Journal of the Mechanics and Physics of Solids*, 38:251–238, 1988.